Synthesis and Characterization of Zeolite–Chitosan Composite from North Toraja Montmorillonite Mineral: Kinetic and Isotherm Study for Cu^{2+} Metal Ion Adsorption

Jumianti Bunga Matande*, Djabal Nur Basir, Paulina Taba, St. Fauziah, Syahruddin Kasim, Hasnah Natsir, Siti Khairunnur, R. Risnawati

Department of Chemistry, Faculty of Mathematics and Natural Science, Hasanuddin University, Makassar, Indonesia

** Corresponding Author. E-mail: djabalnurbasir@unhas.ac.id; telp: +62-85-241911811, authors' email: jumiantibungam@gmail.com, paulinataba@unhas.ac.id , st.fauziah@unhas.ac.id, kasimsyahruddin1@gmail.com, hasnanatsir@unhas.ac.id, skhairunnur@gmail.com, risnawatiiiiy@gmail.com*

Abstract

Natural montmorillonite from North Toraja, rich in silica and alumina, was employed as a precursor for synthesize cancrinite-type zeolite (CAN) through hydrothermal treatment at 170 °C for 24 h in 5 M NaOH solution. Zeolite, a porous aluminosilicate material widely applied in wastewater treatment, especially for heavy metal ion adsorption. To enhance adsorption performance, CAN was modified with chitosan through phase inversion, resulting in the formation of a zeolite–chitosan composite. Characterization using XRD, FTIR, SEM EDS, BET, and TGA DSC. XRD analysis revealed diffraction peaks at 2θ = 13.94°, 18.84°, 21.28°, 24.16°, 27.34°, 32.42°, 34.32°, 36.76°, and 42.46°. FTIR confirmed functional groups of CANat 678, 624, and 563 cm^{-1} and chitosan at 2879, 1643 cm^{-1}. SEM revealed a morphological change from sharp crystals to rough surface due to chitosan coating, while EDS identified the main elements C, O, Na, Mg, Al, and Si. BET analysis indicated a surface area of 22.12 m^2/g with pore diameter of approximately 28.48 nm. TGA-DSC indicated improved thermal stability, evidenced by a shift in degradation temperature attributed to strong zeolite-

chitosan interaction. Adsorption studies for Cu^{2+} ions demonstrated optimum conditions at pH of 5 with a contact time of 150 min. Kinetic data followed a pseudo-second-order model, while equilibrium was best described by the Sips isotherm, with a maximum adsorption capacity of 360.65 mg/g. These findings confirm that CAN–Chitosan composite derived from North Toraja minerals are efficient and stable adsorbents for heavy metal removal, supporting sustainable wastewater treatment and environmental remediation.

Keywords: Synthesis; Zeolite Cancrinite; Chitosan; Adsorption; Cu^{2+}

1. Introduction

The rapid growth of industries, such as mining, metal plating, and electronics, has led to an increase in liquid waste containing heavy metals [1]. Heavy metals are a serious concern in environmental issues because of their persistent nature, inability to biodegrade (non-biodegradable), and high solubility in water, making them likely to accumulate in the food chain over a long period [2,3]. Clinically, heavy metals are inorganic and carcinogenic [4,5]. Exposure to these metals, even at minimal levels, can result in fatal health risks, including growth disorders, internal organ damage (liver, kidneys, and heart), cancer, to central nervous system disorders and death [6,7,8,9,10]. One of the heavy metal pollutants that requires urgent management is copper (Cu^{2+}). Although copper is an essential trace element required in small amounts by the human body, excessive concentrations can cause toxic effects [11].

Numerous technologies have been employed for the treatment of heavy metal-containing wastewater, encompassing methods from conventional processes to more advanced treatment systems. Conventional methods such as chemical precipitation [12], bioremediation [13], coagulation-flocculation [14], and ion exchange [1] often show limitations, such as inefficiency for waste with high acidity, large sludge production, and high operational costs [15,16]. On the other hand, advanced technologies such as photocatalysis [17,18], electrodialysis [19,20], and membrane filtration [21] offer high efficiency but require expensive investment costs [22]. Therefore, adsorption methods remain the main choice due to their simplicity, high efficiency, relatively low cost, and the reusability of adsorbents

[23,24].

Zeolite is a porous aluminosilicate material with a three-dimensional crystalline structure composed of tetrahedral silica (SiO_2) and alumina (Al_2O_3) units interconnected through oxygen atoms, forming a negatively charged framework that is neutralized by alkali and alkaline earth cations in its pores [25]. The regular porous structure and high surface area make zeolite function as a cation exchanger, adsorbent, and catalyst, with its performance significantly influenced by the Si/Al ratio, which determines the chemical and thermal stability of the material [26]. CANbe obtained naturally or synthesized. However, the use of synthetic zeolite as an adsorbent has better characterization compared to natural zeolite [27]. CANbe synthesized from materials containing silica and alumina, including montmorillonite [25]. The use of local montmorillonite minerals from North Toraja as the main raw material for the synthesis of cancrinite (CAN) zeolite because it contains SiO_2 (56.55%) and Al_2O_3 (37.38%) which support the formation of an aluminosilicate framework.

The use of synthetic zeolite as a metal ion adsorbent has been widely carried out and has shown good results. Several studies indicate that the interaction occurring between the surface of zeolite and metal ions is through cation exchange [28,29]. Moreover, the enhancement of adsorption capacity for several metal ions is also associated with the availability of active sites. To enhance its properties as an adsorbent, zeolite is composited using chitosan. Chitosan is a natural polysaccharide obtained through the deacetylation of chitin, which is the main compound that makes up the exoskeleton of marine organisms such as shrimp and crabs. Chitosan has primary functional groups in the form of amino ($-NH_2$) and hydroxyl (-OH). The presence of these active groups makes chitosan effective in the adsorption process [29]. Several studies have shown that the combination of zeolite and chitosan is capable of removing Cu^{2+} metal ions with high efficiency, reaching 99% [30].

In addition, the study of adsorption kinetics and isotherms becomes an important aspect in understanding the interaction mechanisms between adsorbent and adsorbate. The adsorption kinetics of Cu^{2+} ions on CAN–Chitosan composite generally follow a pseudo-second-order model, which indicates that the adsorption process is controlled by chemical interactions (chemisorption) through electron

exchange or valence bonding [31]. Meanwhile, the adsorption isotherm is better explained by the Sips model, which combines the characteristics of the Langmuir isotherm (monolayer adsorption) and Freundlich (heterogeneous surface), thus being able to describe both the maximum adsorption capacity and the surface heterogeneity [32]. This analysis provides a scientific basis for optimizing operating conditions as well as predicting adsorption capacity at an industrial scale.

Thus, this study aims to produce a CAN–Chitosan composite-based adsorbent material that has better structural stability, selectivity, and adsorption efficiency compared to single zeolite. The development of this adsorbent material is expected to provide a more efficient and economical innovative solution for removing heavy metal ions Cu^{2+} from aquatic environments, especially mining industry waste. Furthermore, the utilization of local minerals, in the form of North Toraja montmorillonite, as the main raw material is expected to increase the usefulness of local natural resources and support the development of sustainable and environmentally friendly waste treatment technology.

2. Materials and Methods

2.1 Material

The materials used in this study are cancrinite zeolite, chitosan (80% deacetylation Sigma-Aldrich), aquabides (OneMed), Whatman-42 filter paper (Merck), universal pH (Merck), NaOH p.a (99% purity, Merck), CH_3COOH (99% purity, Merck), $CuSO_4.5H_2O$ (Merck).

2.2. Synthesis of Cancrinite Zeolite

The zeolite used in this study is cancrinite zeolite (CAN), synthesized following the procedure reported previously [31] with a hydrothermal reaction time at 170℃ for 24 hours. The resulting zeolite was washed until the filtrate reached neutral pH, dried at 100℃ for 24 hours, and then re-characterized using XRD, FTIR, and SEM to confirm the crystalline phase, functional groups, and surface morphology. The obtained zeolite was subsequently prepared for composite fabrication.

2.3. Cancrinite and Chitosan Composite

The Zeolite-chitosan composite (CAN-chitosan) was prepared by dissolving 0.5

g of chitosan in 20 mL of 2% acetic acid for 30 minutes, then adding 2 g of CAN into a 150 mL beaker. The mixture was stirred with a magnetic stirrer for 30 minutes until a homogeneous composite solution formed. Next, the solution was placed into a 10 cc syringe and then slowly dropped into a 1 M NaOH solution until granules formed. The formed granules were separated from the NaOH solution and then dried in an oven at 70°C. After drying, the granules were gently ground into powder and then sieved using a 100 mesh sieve. The composite powder was then rinsed with distilled water until the pH was neutral and dried again in an oven at 70°C. The final product obtained was then characterized using XRD, FTIR, SEM-EDS, SAA (BET BJH), and TGA-DSC.

2.4. Characterization of composite materials

The instruments used in this study include Atomic Absorption Spectrophotometry (AAS) (Buck Scientific Model 205 VGP), to analyze the adsorption process of the composite. X-Ray Diffraction (Shimadzu XRD-700 Maxima) was used to determine the crystal structure and phase identity as well as the diffraction angle (2θ) values of cancrinite zeolite and zeolite-chitosan composite. Data collection was carried out in the 2θ range between 15° and 70° using a scanning rate of 2° per minute with a Cu-Kα radiation source. FTIR spectra were obtained using Shimadzu IR Prestige 21 to identify the presence of specific functional groups in zeolite-chitosan, focusing on the shift in wavenumber in the 400–4000 cm-1 region with sample preparation using the KBr pellet method. The morphology of the structure and elemental composition were characterized using SEM-EDS, SU-3500 imaging. Nitrogen adsorption-desorption isotherms were obtained using SAA (Altamira Micro200) and surface area was determined using the Brunauer-Emmett-Teller (BET) method. Thermal stability and calorimetric changes in the synthesized material were analyzed using TGA-DSC (Linseis STA PT1600).

2.5. Adsorption Test

The adsorption study of Cu^{2+} ions was carried out using a zeolite–chitosan composite adsorbent. Each experiment was conducted three times to ensure the reliability and reproducibility of the data. In each test, 50 mL of metal ion solution

was placed in an Erlenmeyer flask, then 0.1 g of the zeolite–chitosan composite adsorbent was added. The adsorption process was conducted with variations in operational parameters, including contact time, solution pH, and initial metal ion concentration (Table 1). The mixture was stirred at room temperature using an MPS-20 orbital shaker at a speed of 130 rpm to ensure homogeneous contact between the adsorbent and adsorbate. After the adsorption process was completed, the mixture was filtered using Whatman No. 42 filter paper, and the obtained filtrate was analyzed using Atomic Absorption Spectroscopy (AAS) to determine the residual concentrations of Cu^{2+} ions in the solution. The adsorbed amounts were calculated using Equations (1).

$$q_e = \frac{C_0 - C_e}{M} \times V \quad (1)$$

Where q_e is adsorption capacity (mg/g), C_0 and C_e are initial and final concentration (mg/L), V is volume of the solution (L), and M is the mass of the adsorbent (g) [32].

In addition, the competitive interaction of Cu^{2+} ions were studied through a ternary metal ion system by mixing 50 mL of each metal ion solution under the previously obtained optimum adsorption conditions. Then, the feasibility of applying the zeolite–chitosan composite was evaluated using real mining wastewater from Southeast Sulawesi to assess its potential for environmental remediation.

2.6. Adsorption Kinetics

Adsorption kinetics is intended to analyze the rate or speed and mechanism of the adsorption process, as can be seen in (equations 2 and 3) [33].

Pseudo First Order (PFO) Model

$$\ln(q_e - q_t) = \ln q_e - k1 \quad (2)$$

Second Order Pseudo Model (PSO)

$$\frac{t}{q_t} = \frac{1}{k_2 {q_e}^2} + \frac{t}{q_e} \quad (3)$$

Where q_e is the amount of ions adsorbed per unit mass of adsorbent (mg/g), q_t is adsorption capacity at time t (mg/g), k_1 is pseudo first order adsorption rate

constant (min^{-1}), t is time (min), and k_2 is pseudo second order adsorption rate constant (min^{-1}).

2.7. Adsorption Isotherms

The adsorption capacity of CAN-Chitosan zeolite composite can be determined using adsorption isotherms. The adsorption isotherm models used are the Langmuir model (monolayer), Freundlich model (multilayer), and Sips model (combination) as in equations (4) to (9).

The linear and nonlinear Langmuir isotherms can be written respectively in equations (4) and (5):

$$\frac{C_e}{q_e} = \frac{1}{q_{max}\,.\,K_L} + \frac{C_e}{q_{max}} \quad (4)$$

$$q_e = \frac{q_{max}\ K_L\ C_e}{1 + K_L\ C_e} \quad (5)$$

Where q_m is maximum Langmuir adsorption capacity (monolayer capacity) (mg/g), K_L is Langmuir constant related to adsorption affinity (L/mg).

Linear and nonlinear Freundlich isotherms can be written respectively in equations (6) and (7):

$$log\ q_e = \log K_F + \frac{1}{n}\log C_e \quad (6)$$

$$q_e = K_F . C_e^{1/n} \quad (7)$$

Where q_e is the amount of ions adsorbed per unit mass of adsorbent (mg/g), K_F is the Freundlich constant indicating adsorption capacity $(L/mg)^{1/n}$, C_e is ion concentration at equilibrium after adsorption (mg/L), and 1/n is heterogeneity exponent.

Linear and nonlinear Sips isotherms can be written, respectively, in equations (8) and (9):

$$\ln\left(\frac{q_e}{q_{max} - q_e}\right) = \ln K_S + \frac{1}{n}\ln C_e \quad (8)$$

$$q_e = \frac{q_{max}\,(K_S\,C_e)^{ns}}{1 + (K_S\,C_e)^{ns}} \quad (9)$$

2.8. Adsorption selectivity

The adsorption selectivity value (K_d) is calculated using equation (10).

$$K_d = \frac{C_0 - C_e}{C_e} \times \frac{v}{m_s} \quad (10)$$

Where C_0 is metal ion concentration before adsorption (mg/L), C_e is ion concentration at equilibrium after adsorption (mg/L), m is adsorbent mass (g), and v is volume of desorption solution (L).

3. Results and Discussion

3.1. Characterization of zeolite CAN-Chitosan composite

The X-ray diffraction (XRD) patterns of CAN–chitosan, chitosan, and CAN are presented in Figure 1. The diffraction pattern of CAN (Figure 1(c)) is dominated by the characteristic reflections of cancrinite at 2θ values of 13.94°, 18.84°, 21.28°, 24.16°, 27.34°, 32.42°, 34.32°, 36.76°, and 42.46°, corresponding to the (110), (101), (210), (300), (211), (400), (311), (102), and (411) crystallographic planes, respectively, which are characteristic of the hexagonal cancrinite structure according to JCPDS No. 96-900-5612. The sharp and well-defined diffraction peaks indicate the successful formation of a highly crystalline cancrinite framework.

In contrast, the diffraction pattern of chitosan (Figure 1(b)) exhibits a broad diffraction peak centered around 2θ ≈ 20°, reflecting its semi-crystalline nature with a predominantly amorphous phase. This behavior is attributed to the irregular arrangement of polymer chains and the presence of intermolecular hydrogen bonding within the chitosan structure [35]. Due to its amorphous character, chitosan exhibits relatively low diffraction intensity and appears as a broad halo, making its diffraction features less pronounced when combined with highly crystalline materials.

For the CAN–Chitosan composite (Figure 1(a)), the characteristic diffraction peaks of cancrinite remain observable at approximately 2θ = 13.82° (110), 18.08° (101), 21.26° (210), 24.14° (300), 27.32° (211), and 42.40° (411), indicating that the aluminosilicate framework of CAN was preserved after the composite formation process. However, the intensities of these peaks decreased compared with those of pristine CAN, suggesting that the zeolite crystals were partially coated by the chitosan matrix, resulting in attenuation of the diffraction signals. Such a reduction in peak intensity is commonly observed in hybrid materials, where

polymer layers cover the surface of crystalline particles without significantly altering their crystal structure [34].

The absence of distinct chitosan diffraction peaks in the composite can be attributed to the dominance of the highly crystalline CAN phase, whose diffraction intensity is substantially greater than that of the semi-crystalline chitosan phase. Since XRD peak intensity is strongly influenced by the relative abundance and crystallinity of the constituent phases, the broad amorphous contribution of chitosan becomes less discernible in the composite pattern. The coexistence of the characteristic cancrinite reflections and the amorphous contribution of chitosan confirms the successful formation of a structurally stable CAN–Chitosan hybrid material.

Furthermore, the preservation of the characteristic cancrinite reflections after composite formation indicates that the crystallographic structure of CAN remained largely unchanged. These findings suggest that the incorporation of chitosan did not significantly affect the crystal framework of the zeolite but rather occurred through interactions at the material surface. Similar observations have been reported for other zeolite-based composites, where the composite preparation process preserved the crystalline zeolite framework while introducing polymeric functional groups onto the surface [36]. Therefore, the retention of the characteristic cancrinite diffraction peaks demonstrates that the structural integrity of CAN was maintained following chitosan incorporation, confirming the successful fabrication of the CAN–Chitosan composite without compromising the fundamental framework of either component [37].

The FTIR spectrum of the CAN–Chitosan composite is presented in Figure 2. A broad absorption band centered at 3452 cm^{-1} is assigned to the overlapping stretching vibrations of hydroxyl (–OH) and amino (–NH) groups originating from chitosan [38]. Compared with pristine CAN, this band becomes broader and more intense, indicating the formation of hydrogen-bonding interactions between the hydroxyl groups on the zeolite surface and the amino and hydroxyl groups of chitosan. These interactions suggest that chitosan is chemically integrated with the zeolite rather than simply physically mixed.

An absorption band at 2879 cm^{-1}, corresponding to the C–H stretching vibration of the polysaccharide backbone, appears only in the composite spectrum and is

absent in pristine CAN, providing further evidence of successful chitosan incorporation. Meanwhile, the absorption band at 1643 cm^{-1} is attributed to the amide I vibration of chitosan, confirming that the polymer backbone remained structurally intact during the composite synthesis process [39]. In addition to the amide band, the CAN–Chitosan composite exhibited characteristic absorption bands at 1483, 1381, and 1338 cm^{-1}, which are assigned to the deformation vibration of amino groups ($–NH_2$), the symmetric deformation of methyl/methylene groups ($–CH_3$/$–CH_2$), and the combined C–N stretching and O–H bending vibrations associated with the polysaccharide structure of chitosan, respectively. Compared with pure chitosan, which exhibited corresponding bands at 1423, 1379, and 1321 cm^{-1}, slight shifts in the band positions were observed after composite formation. These spectral shifts indicate changes in the chemical environment surrounding the amino and hydroxyl functional groups, suggesting intermolecular interactions between chitosan and the aluminosilicate framework of CAN through hydrogen bonding and electrostatic interactions. Importantly, despite these minor shifts, all characteristic functional groups of chitosan remained clearly identifiable, indicating that the chemical structure of chitosan was preserved during composite formation while successfully interacting with the zeolite framework.

The characteristic band at 991 cm^{-1} is assigned to the asymmetric stretching vibration of the Si–O–Al framework of CAN [40]. The retention of this band after composite formation indicates that the crystalline aluminosilicate framework remains intact following chitosan incorporation. Likewise, the characteristic CAN triplet bands at 680, 624, and 565 cm^{-1} [41] are clearly preserved in the composite spectrum, confirming that the cancrinite framework is maintained throughout the synthesis process.

Overall, the FTIR results confirm the successful fabrication of the CAN–Chitosan composite through the coexistence of characteristic functional groups derived from both chitosan and CAN. The composite combines the chemically active functional groups of chitosan with the stable aluminosilicate framework of CAN, providing multiple adsorption sites for Cu^{2+}. Consequently, the adsorption performance of the composite is governed not only by its textural properties but also by the synergistic contribution of these chemically active sites. The amino and hydroxyl groups of chitosan can coordinate Cu^{2+} ions through surface complexation

and chelation, whereas the negatively charged aluminosilicate framework contributes through electrostatic attraction and ion-exchange mechanisms. This synergistic effect explains why the CAN–Chitosan composite exhibits enhanced Cu^{2+} adsorption performance despite possessing a lower BET surface area than pristine CAN.

To further elucidate the adsorption mechanism, the FTIR spectra of the CAN–Chitosan composite before and after Cu^{2+} adsorption were compared, as shown in Figure 3. Distinct shifts in both the position and profile of several characteristic absorption bands were observed after adsorption, confirming the involvement of multiple functional groups in Cu^{2+} binding. The broad –OH/–NH stretching band shifted from 3452 to 3444 cm^{-1}, accompanied by slight broadening and reduced intensity, indicating the direct participation of hydroxyl and amino groups in Cu^{2+} coordination through coordination bonding and hydrogen-bond rearrangement. Likewise, the C–H stretching band shifted from 2879 to 2887 cm^{-1}, suggesting subtle changes in the chemical environment of the chitosan backbone following metal uptake.

The amide band also shifted from 1643 to 1639 cm^{-1}, indicating the involvement of carbonyl and adjacent amino groups in Cu^{2+} adsorption. Such spectral shifts are characteristic of coordination between Cu^{2+} ions and the lone-pair electrons of nitrogen and oxygen atoms in chitosan, resulting in the formation of stable surface complexes. The simultaneous shifts of the hydroxyl, amino, and amide bands therefore demonstrate that chitosan serves as the primary coordination matrix for Cu^{2+} adsorption.

In addition to the changes associated with chitosan, significant spectral variations were observed in the zeolite framework. The Si–O–Al stretching band shifted from 991 to 1008 cm^{-1}, while the characteristic CAN bands at 680, 624, and 565 cm^{-1} shifted to 671, 623, and 557 cm^{-1}, respectively. These shifts indicate that Cu^{2+} adsorption also affects the aluminosilicate framework, suggesting the occurrence of electrostatic interactions and partial ion exchange between Cu^{2+} ions and the exchangeable cations within the CAN structure. The slight distortion of the framework vibrations further demonstrates that the zeolite matrix actively participates in the adsorption process.

Overall, the FTIR results demonstrate that Cu^{2+} adsorption onto the CAN–

Chitosan composite proceeds through a synergistic dual adsorption mechanism involving both the organic and inorganic components of the composite. Chitosan provides abundant amino, hydroxyl, and amide groups that bind Cu^{2+} through coordination and chelation, whereas the negatively charged aluminosilicate framework of CAN facilitates electrostatic attraction and ion exchange. The simultaneous spectral shifts observed in both the organic functional groups and the zeolite framework provide compelling evidence for the cooperative contribution of these two components during adsorption. These findings are consistent with previous studies [40] which reported the coordination of Cu^{2+} with amino and hydroxyl groups in zeolite–chitosan composites, and [42], which observed similar shifts in aluminosilicate framework vibrations after Cu^{2+} adsorption. Collectively, these results demonstrate that the superior adsorption performance of the CAN–Chitosan composite originates from the synergistic interaction between the chemically active functional groups of chitosan and the ion-exchange capacity of the CAN framework, rather than from surface area alone.

The morphology of the CAN-Chitosan composite is shown in Figure 4 at 10,000 and 20,000x magnification. Figure 4a and 4b show the morphology of the CAN, which is shaped like a long rod. Araujo et al. showed that the zeolite-chitosan composite has an irregular morphology and has many flakes on its surface [43]. Figure 4c and 4d still have the morphology of CAN, but mostly have an irregular morphology, so it can be seen that CAN has bonded with the chitosan framework to form a composite.

Energy Dispersive Spectroscopy (EDS) analysis of CAN–Chitosan composite Figure 5 shows that the main elements detected consist of C (28.37%), O (48.13%), Na (7.41%), Mg (1.20%), Al (6.11%), and Si (8.79%), indicating the successful formation of an organic–inorganic composite material. The relatively high carbon content comes from chitosan as the polymer matrix, while oxygen originates from both constituent components. The presence of Si and Al confirms the existence of the typical aluminosilicate framework of zeolite composed of SiO_4 and AlO_4 tetrahedral units, whereas Na and Mg act as balancing cations in the zeolite structure. The combination of these elements indicates that chitosan has successfully integrated with the zeolite without altering the basic composition of its crystal framework. These results are consistent with various studies reporting

that zeolite–chitosan composites are generally dominated by the elements C, O, Si, and Al as indicators of successful synthesis and material integration [40, 44].

Based on BET and BJH analyses Table 2, pure CAN exhibits a higher specific surface area (43.03 m^2/g) compared to the CAN–Chitosan composite (22.12 m^2/g), indicating that the incorporation of chitosan partially blocks the surface and micropores of the zeolite, thereby reducing the accessible active sites for N_2 molecules. Nevertheless, the total pore volume and median pore diameter increase significantly in the CAN–Chitosan composite, from 0.07363 to 0.08354 cm^3/g and from 10.55 to 28.48 nm, respectively. This shift suggests a transition in porosity characteristics from micropore dominance to mesopore formation, attributed to the development of interparticle voids and pore networks derived from the chitosan matrix. Such phenomena are commonly reported in zeolite–biopolymer composites, where polymer coating or impregnation reduces the specific surface area but enhances pore size and volume, making the material more suitable for adsorption of metal ions or larger molecules. Similar trends have been reported by [45], which demonstrated that chitosan integration into zeolite structures promotes mesoporosity at the expense of BET surface area.

Nitrogen adsorption–desorption isotherms (Figure 6) further confirm these textural changes. Both CAN and the CAN–Chitosan composite exhibited type IV isotherms according to the IUPAC classification, accompanied by H4-type hysteresis loops, indicating the presence of mesoporous structures and slit-shaped pores characteristic of zeolite-based composite materials. The pore size distribution profiles also revealed that CAN possessed a relatively narrow pore distribution (approximately 4–10 nm), whereas the CAN–Chitosan composite exhibited a broader distribution with larger pore diameters, reflecting the formation of a more heterogeneous pore network after composite preparation [46].

Although the BET surface area decreased following chitosan incorporation, the adsorption performance of the CAN–Chitosan composite cannot be explained solely by its textural properties. The introduction of chitosan provides additional amino ($–NH_2$) and hydroxyl (–OH) functional groups that serve as active binding sites for Cu^{2+} ions. These functional groups can interact with metal ions through electrostatic attraction, ion exchange, surface complexation, and chelation mechanisms. Therefore, the adsorption capacity of the composite is governed not

only by the available surface area but also by the abundance of chemically active functional groups. Moreover, the increase in pore diameter and pore volume enhances the accessibility of Cu^{2+} ions to the adsorption sites located within the composite structure.

These results suggest that the incorporation of chitosan modifies the adsorption mechanism from one primarily controlled by the physical characteristics of the zeolite surface to a synergistic process involving both textural properties and chemical interactions. Consequently, despite exhibiting a lower BET surface area than pristine CAN, the CAN–Chitosan composite possesses enhanced adsorption functionality due to the combined effects of mesopore development and the presence of additional metal-binding functional groups.

Based on the TGA–DSC analysis of the CAN–Chitosan composite (Figure 7), three main thermal events were observed. In the low-temperature region (30–120°C), the DSC curve exhibited an endothermic peak with a maximum temperature of 79.61°C and an onset temperature of 49.66°C, accompanied by an enthalpy change of +35.34 J/g. This thermal event is attributed to the evaporation of physically adsorbed water and bound water molecules present on the chitosan surface as well as within the microporous structure of CAN [47]. The TGA curve revealed a weight loss of approximately 4% within this temperature range, confirming the release of moisture associated with hydroxyl (–OH) and amino (–NH_2) groups through hydrogen-bonding interactions. Similar behavior has been reported for chitosan-based materials, where weight loss below 150°C is primarily associated with the removal of adsorbed and physically bound water [48]. Furthermore, the porous aluminosilicate framework of zeolite contributes to water retention, resulting in the observed thermal behavior [49]. The relatively high positive enthalpy value indicates that a considerable amount of energy is required to remove water molecules strongly associated with the hydrophilic functional groups and zeolite pores.

In the temperature range of 250–350°C, the DSC curve displayed an exothermic peak with a maximum temperature of 316.92°C and an onset temperature of 304.53°C, corresponding to an enthalpy change of −12.05 J/g. This stage represents the primary thermal degradation process of chitosan and is associated with the cleavage of glycosidic bonds, depolymerization, and deacetylation reactions. The

TGA profile showed the most significant weight loss during this stage, amounting to approximately 9%, indicating the decomposition of the organic polymer matrix and the formation of volatile products such as CO_2, NH_3, and H_2O [48,50]. The degradation temperature of the CAN–Chitosan composite was higher than that generally reported for pure chitosan, suggesting enhanced thermal stability following composite formation. This behavior may be attributed to hydrogen bonding and electrostatic interactions between the amino groups of chitosan and the active sites on the CAN surface, which restrict polymer chain mobility and delay thermal decomposition.

At temperatures above 350°C up to 600°C, the weight loss became more gradual, indicating the carbonization of residual organic matter and the formation of amorphous carbon (char). In this region, the TGA curve showed an additional weight loss of approximately 5%, while the residual mass remained around 75% at 600°C. The high residual mass demonstrates the excellent thermal stability of the inorganic CAN framework, which does not undergo significant decomposition within the investigated temperature range. The presence of thermally stable aluminosilicate structures contributes to an increased char yield and suppresses further degradation of the composite [51].

Overall, the TGA–DSC results demonstrate that the CAN–Chitosan composite possesses good thermal stability, characterized by limited moisture loss at low temperatures, delayed degradation of the chitosan phase at elevated temperatures, and a high residual mass at high temperatures. These findings confirm that the incorporation of CAN enhances the thermal resistance of chitosan and contributes to the formation of a thermally stable hybrid material.

3.2. The Effect of Adsorption Time of Cu^{2+} Metal Ions by CAN-Chitosan Composite

Figure 8 illustrates the effect of contact time on the adsorption of Cu^{2+} ions by CAN and the CAN–chitosan composite. For both adsorbents, the adsorption capacity (q_e) increased rapidly during the initial stage of adsorption and gradually approached equilibrium with increasing contact time. The rapid adsorption observed during the first 5–30 min is attributed to the abundance of available active sites on the adsorbent surface, including amino ($–NH_2$) and hydroxyl (–OH)

functional groups from chitosan, as well as cation-exchange sites within the CAN framework. These active sites facilitate the adsorption of Cu^{2+} ions through ion-exchange, surface complexation, and electrostatic interactions [53].

For the CAN–chitosan composite, the adsorption capacity increased from 24.48 mg g^{-1} at 5 min to 37.95 mg g^{-1} at 30 min, followed by a slower increase to 48.08 mg g^{-1} at 120 min. The reduced adsorption rate at longer contact times indicates the progressive occupation of active adsorption sites by Cu^{2+} ions, resulting in fewer available binding sites and increased diffusion resistance toward the internal pores of the adsorbent. After 150 min, the adsorption capacity remained nearly constant, varying only from 48.76 to 48.73 mg g^{-1} up to 180 min, indicating that adsorption equilibrium had been achieved. Therefore, the optimum contact time for Cu^{2+} adsorption using the CAN–chitosan composite was determined to be 150 min, corresponding to a maximum adsorption capacity of 48.76 mg g^{-1} [54].

A similar adsorption behavior was observed for the pristine CAN adsorbent, although equilibrium was reached earlier at approximately 90 min. The shorter equilibrium time suggests that adsorption on CAN is primarily governed by cation exchange within the zeolite framework. In contrast, the CAN–chitosan composite required a longer equilibrium time (150 min), which can be attributed to the additional adsorption mechanisms introduced by the chitosan coating. Besides ion exchange, Cu^{2+} ions interact with the amino and hydroxyl groups through coordination and complexation, leading to a higher adsorption capacity but a slightly longer time to achieve equilibrium. These results demonstrate the synergistic effect of combining CAN with chitosan, which enhances the overall adsorption performance toward Cu^{2+} ions despite extending the equilibrium time.

3.3. Adsorption Kinetics

Adsorption kinetics describes the relationship between contact time and the rate of the adsorption process, which represents the change in the amount of adsorbate until equilibrium is reached [55]. Kinetic models are not only used to assess the adsorption rate, but also provide insight into the mechanisms occurring during the process [56].

Figures 9 present the fitting of the experimental data using the pseudo-first-order (PFO) and pseudo-second-order (PSO) kinetic models, while the

corresponding kinetic parameters are summarized in Table 3. The PSO model provided a significantly better fit than the PFO model, as evidenced by the higher coefficient of determination (R^2 = 0.9995 for CAN–Chitosan and 0.9993 for CAN), whereas the PFO model exhibited lower R^2 values of 0.8929 and 0.7655, respectively. Moreover, the equilibrium adsorption capacities (q_e) predicted by the PSO model (51.0204 and 51.8135 mg g^{-1}) were in good agreement with the experimental values (48.7598 and 50.5894 mg g^{-1}), while those obtained from the PFO model deviated considerably. These results indicate that the adsorption of Cu^{2+} on both CAN and the CAN–Chitosan composite is better described by the PSO model, suggesting that the adsorption process is predominantly governed by chemisorption involving ion exchange and complexation with the active functional groups of the adsorbent [57]. Similar findings have been reported for chitosan- and zeolite-based adsorbents, where heavy metal adsorption generally follows pseudo-second-order kinetics [58].

3.4. Effect of pH

The degree of acidity (pH) is an important factor that affects the adsorption process of metal ions in solution. Based on research results shown in (Figure 10), an increase in pH from 2 to 5 demonstrates a significant rise in the adsorption capacity (q_e) of Cu^{2+} ions by the CAN–Chitosan composite, which then decreases at higher pH. Under acidic conditions (pH 2 and 3), the low adsorption capacity is caused by the dominance of H^+ ions competing with metal ions to bind with the active groups of the adsorbent, especially the amino groups ($–NH_2$) on chitosan which are protonated to $–NH_3^+$, thus reducing the coordination ability towards metals. As the pH increases towards the optimum condition (pH 4–5), the functional groups undergo deprotonation, increasing the availability of free electron pairs on $–NH_2$ and –OH, as well as enhancing the negative charges on the zeolite framework ($Si–O^-$ and $Al–O^-$), which promotes adsorption mechanisms through chelation, surface complexation, and ion exchange. This condition results in maximum adsorption capacity, especially for Cu^{2+}, which shows the highest affinity for nitrogen and oxygen donor groups. At pH above 5, a decrease in adsorption capacity occurs due to the formation of metal hydroxide species such as $Cu(OH)_2$ which precipitate, thus shifting the mechanism from adsorption to

precipitation [43,58].

The pH of the solution is one of the important parameters in the adsorption process, besides contact time. The pH of the solution can affect the charge of active sites on the adsorbent and the interaction between adsorbent and adsorbate [38, 39]. Fig. 10 shows that as the pH increases, the adsorption capacity of Cu^{2+} ions also increases until the optimum pH is 5. This is due to strong acidic conditions. At low pH, there are many H^+ ions that interact with active sites on the adsorbent surface, reducing the adsorption capacity of Cu^{2+} ions. However, as the pH increases, the concentration of H^+ ions decreases, and the protonated active sites are deprotonated so as to increase the adsorption capacity of Cu^{2+} ions [40].

3.5. The effect of concentration and Adsorption Isotherms

Adsorption isotherms describe the equilibrium relationship between the concentration of adsorbate remaining in solution and the amount adsorbed onto the adsorbent surface at constant temperature [60]. Isotherm parameters provide valuable information regarding the adsorption mechanism, surface characteristics, adsorption affinity, and maximum adsorption capacity of the adsorbent [61]. The adsorption isotherms of Cu^{2+} ions onto CAN and the CAN–chitosan composite are presented in Figure 11, while the corresponding parameters obtained from linear and non-linear isotherm models are summarized in Tables 4 and 5, respectively.

As shown in Figure 11, the adsorption capacity of both CAN and the CAN–chitosan composite increased progressively with increasing equilibrium concentration (C_e). For CAN, the adsorption capacity increased from 49.681 to 81.859 mg g^{-1}, whereas the CAN–chitosan composite exhibited an increase from 48.062 to 83.913 mg g^{-1} within the initial Cu^{2+} concentration range of 50–300 mg L^{-1}. This behavior indicates that a higher Cu^{2+} concentration enhances the concentration gradient between the solution and the adsorbent surface, thereby increasing the mass transfer driving force and promoting diffusion of Cu^{2+} ions into the external surface and internal pores of the adsorbent. Since adsorption saturation was not reached within the investigated concentration range, a considerable number of active adsorption sites remained available for Cu^{2+} uptake.

The equilibrium data for CAN were analyzed using the Langmuir and

Freundlich isotherm models, whereas the CAN–chitosan composite was further evaluated using the Langmuir, Freundlich, and Sips models in both linear and non-linear forms. The linear fitting results (Table 4) indicate that both Langmuir and Freundlich models adequately describe the adsorption equilibrium, with coefficients of determination (R^2) greater than 0.98 for both adsorbents. For CAN, the Langmuir model yielded an R^2 value of 0.9816 and a maximum adsorption capacity (qm) of 78.1250 mg g^{-1} (1.2294 mmol g^{-1}), while the CAN–chitosan composite exhibited a higher R^2 value of 0.9898 with a qm of 82.6446 mg g^{-1} (1.3006 mmol g^{-1}). These results indicate that Cu^{2+} adsorption can be reasonably described by monolayer adsorption on energetically uniform active sites, consistent with the fundamental assumptions of the Langmuir isotherm [62].

The higher adsorption capacity of the CAN–chitosan composite compared with pristine CAN demonstrates the beneficial effect of chitosan modification. Although the Langmuir affinity constant (KL) of CAN (0.2500 L mg^{-1}) was slightly higher than that of the composite (0.1885 L mg^{-1}), the composite exhibited a greater adsorption capacity. This finding suggests that the adsorption performance is governed not only by adsorption affinity but also by the number and accessibility of active adsorption sites. The incorporation of chitosan introduces abundant amino ($–NH_2$) and hydroxyl (–OH) functional groups, which act as additional coordination sites for Cu^{2+} ions through surface complexation, while the CAN framework simultaneously provides negatively charged aluminosilicate sites capable of ion exchange. The synergistic contribution of these two adsorption mechanisms is responsible for the enhanced adsorption performance of the composite.

The Freundlich model also provided an excellent description of the equilibrium data, with R^2 values of 0.9894 for CAN and 0.9948 for the CAN–chitosan composite. The Freundlich constants (KF) of 42.4522 and 39.5367 L g^{-1}, together with nF values of 8.1633 and 7.0472, respectively, indicate favorable adsorption because nF > 1 [63]. The superior fit of the Freundlich model for the composite suggests that Cu^{2+} adsorption occurs on a heterogeneous surface with adsorption sites possessing different binding energies. Such heterogeneity originates from the coexistence of ion-exchange sites within the CAN framework and amino and hydroxyl functional groups introduced by chitosan, resulting in multiple adsorption pathways for Cu^{2+} ions.

To further evaluate the adsorption equilibrium, the experimental data for the CAN–chitosan composite were fitted using non-linear Langmuir, Freundlich, and Sips isotherm models (Figure 14), and the fitting parameters are presented in Table 5. The goodness-of-fit was evaluated using the sum of squared residuals (SSR), where lower SSR values indicate better agreement between the experimental data and the model [64]. Among the evaluated models, the Freundlich model exhibited the lowest SSR value (22.4708), followed by the Sips model (30.5811), whereas the Langmuir model produced a considerably higher SSR value (782.5515). These results indicate that the Freundlich model provides the most accurate representation of the adsorption equilibrium, confirming that Cu^{2+} adsorption on the CAN–chitosan composite occurs predominantly on energetically heterogeneous adsorption sites.

The Sips isotherm, which combines the characteristics of the Langmuir and Freundlich models, yielded a heterogeneity parameter (ns) of 0.1755, indicating a highly heterogeneous adsorption surface. However, the theoretical maximum adsorption capacity predicted by the Sips model (qms = 360.6529 mg g^{-1}) was substantially higher than both the experimental adsorption capacity and the Langmuir-derived qm. This discrepancy suggests that the Sips model overestimated the maximum adsorption capacity because of the flexibility of its three-parameter non-linear regression, particularly when the experimental data do not completely reach saturation. Consequently, the Langmuir-derived qm (82.6446 mg g^{-1}) is considered a more realistic estimate of the actual adsorption capacity, whereas the Freundlich model more accurately reflects the heterogeneous nature of the adsorption process [42,64].

Overall, the adsorption isotherm analysis demonstrates that Cu^{2+} adsorption onto the CAN–chitosan composite is governed by a synergistic combination of ion exchange within the cancrinite (CAN) framework and surface complexation through the amino ($–NH_2$) and hydroxyl (–OH) functional groups of chitosan. The CAN framework provides a negatively charged aluminosilicate structure with exchangeable Na^+ ions that facilitate cation exchange, while chitosan contributes additional functional groups capable of forming stable coordination complexes with Cu^{2+} ions. This synergistic interaction significantly enhances the adsorption capacity of the CAN–chitosan composite compared with pristine CAN, highlighting

its potential as an efficient adsorbent for the removal of Cu^{2+} ions from contaminated aqueous solutions.

The comparison presented in (Table 6) demonstrates that the CAN–Chitosan composite developed in this study exhibits a superior adsorption capacity for Cu^{2+} ions compared with several previously reported adsorbents. Conventional zeolite-based adsorbents, including NaP1, NaP, zeolite 4A, and SCDO, exhibit adsorption capacities of 14.60, 42.90, 61.64, and 24.32 $mg.g^{-1}$, respectively [74,75,53,76]. In contrast, the synthesized cancrinite (CAN) achieved an adsorption capacity of 78.125 mg g^{-1}, while the CAN–Chitosan composite further increased the capacity to 82.6446 mg g^{-1}. This enhancement is attributed to the synergistic effect between the cancrinite framework, which provides abundant ion-exchange sites, and the amino ($–NH_2$) and hydroxyl (–OH) functional groups of chitosan, which promote Cu^{2+} adsorption through surface complexation in addition to ion-exchange. The superior adsorption performance demonstrates the effectiveness of the CAN–Chitosan composite for Cu^{2+} removal and highlights its strong potential as an efficient adsorbent for practical wastewater treatment applications.

3.6. Adsorption selectivity

Figure 14 shows the distribution constant (K_d) values for Cu^{2+}, Cd^{2+}, Mn^{2+}, and Zn^{2+} ions under optimum Cu^{2+} conditions, which are used to evaluate the selectivity of zeolite–chitosan adsorbent in a multimetal system. In general, higher K_d values indicate a stronger adsorption affinity for a particular ion. The study results show that under optimum Cu^{2+} conditions, the K_d value of Cu^{2+} reaches 5.6, much higher compared to Cd^{2+} (1.83), Zn^{2+} (2.05), and Mn^{2+} (1.69), indicating that the zeolite–chitosan adsorbent has high selectivity toward Cu^{2+}, although other ions can still interact with the adsorbent's active sites. This selectivity is related to the physicochemical properties of Cu^{2+}, which has lower hydration energy and a smaller hydration radius, making it easier to undergo dehydration and bind to $–NH_2$ and –OH groups on chitosan through chelation and surface complexation mechanisms [43, 58]. In addition, the contribution of the negatively charged zeolite framework ($Si–O^-$ and $Al–O^-$) also strengthens the electrostatic interaction between Cu^{2+} and the adsorbent, thereby significantly increasing the K_d value [38].

3.7. Application on Liquid Waste from the Mining Industry

The application of the CAN–Chitosan composite to real mining wastewater collected from Southeast Sulawesi was evaluated by determining the distribution coefficient (Kd) together with the removal efficiency of Cu^{2+} ions (Figure 15). To further validate the adsorption performance under real wastewater conditions, the initial concentration (C_0), equilibrium concentration (C_e), and removal efficiency were also evaluated. The initial Cu^{2+} concentration in the wastewater sample was 12.35589 mg L^{-1}, which decreased to 0.11028–0.20426 mg L^{-1} after adsorption, with an average equilibrium concentration of 0.16249 mg L^{-1}. This substantial decrease resulted in a Cu^{2+} removal efficiency of 98.35–99.11%, with an average value of 98.68%, demonstrating that the CAN–Chitosan composite was capable of removing nearly all Cu^{2+} ions from the real wastewater sample. The high removal efficiency is consistent with the distribution coefficient (Kd = 39.86), indicating a very strong affinity of the composite toward Cu^{2+} under complex wastewater conditions. These findings demonstrate that, in addition to exhibiting excellent adsorption performance in synthetic solutions, the CAN–Chitosan composite also performs remarkably well in the treatment of real mining wastewater.

The distribution coefficient (Kd) represents the affinity of the adsorbent for metal ions, where a higher Kd value corresponds to stronger adsorption and greater separation efficiency. As shown in Figure 14, Cu^{2+} exhibited a substantially higher Kd value (39.86) than Cd^{2+} (0.49) and Mn^{2+} (0.13), indicating that the CAN–Chitosan composite possesses remarkable selectivity toward Cu^{2+} in multicomponent wastewater systems. In contrast, the relatively low Kd values of Cd^{2+} and Mn^{2+} suggest weaker adsorption under identical conditions. This behavior is consistent with the physicochemical properties of these metal ions, particularly their hydration energy, hydrated ionic radius, and electronegativity. Cu^{2+} possesses a relatively lower hydration energy and a smaller hydrated radius, facilitating partial dehydration and enabling stronger interactions with the amino ($–NH_2$) and hydroxyl (–OH) groups of chitosan as well as the negatively charged Si–O–Al framework of CAN [68]. Furthermore, according to the Hard and Soft Acids and Bases (HSAB) theory, Cu^{2+} exhibits a stronger tendency to coordinate with nitrogen- and oxygen-containing donor atoms than Mn^{2+}, thereby enhancing its competitive adsorption in multimetal systems. In addition, Cd^{2+} and Mn^{2+} tend to

undergo partial hydroxide precipitation under near-neutral conditions, reducing their dissolved concentrations and consequently decreasing their adsorption efficiencies [43].

The adsorption behavior observed in this study is further supported by the geological and environmental characteristics of Southeast Sulawesi, one of Indonesia's major mining regions, which is rich in copper-, nickel-, and gold-bearing mineral deposits [69]. Mining activities in areas such as Pomalaa and Konawe generate wastewater containing multiple heavy metals with varying concentrations and complex chemical compositions [70]. Moreover, studies conducted on the Pesouha River have demonstrated that mining effluents contain diverse dissolved metal species that compete for available adsorption sites within aquatic systems [71]. Under these competitive conditions, ions with higher affinity toward the adsorbent, such as Cu^{2+}, preferentially occupy the available active sites, resulting in significantly higher Kd values than those observed for Cd^{2+} and Mn^{2+}.

The superior selectivity of the CAN–Chitosan composite toward Cu^{2+} is also consistent with previous environmental studies conducted in Sulawesi, which demonstrated that the distribution and mobility of heavy metals are strongly governed by the intrinsic chemical properties of each ion together with the physicochemical characteristics of the surrounding aquatic environment [72]. Overall, these findings confirm that the adsorption performance observed under laboratory conditions is representative of real mining wastewater systems and further demonstrate the considerable potential of the CAN–Chitosan composite as a highly selective and efficient adsorbent for Cu^{2+} removal from mining wastewater.

3.8. Conclusions

The CAN–Chitosan composite has been successfully developed as a stable organic–inorganic adsorbent with enhanced mesoporous characteristics and a high affinity for Cu^{2+} ions. The incorporation of chitosan into the CAN framework modifies the texture and surface properties of the material without damaging the crystal structure, thereby increasing the accessibility of active adsorption sites. Adsorption studies indicate that Cu^{2+} removal is largely governed by chemisorption through ion exchange and surface complexation mechanisms, while isotherm analysis confirms that adsorption occurs on heterogeneous surfaces with combined monolayer and multilayer interactions, best represented by the Sips model.

Compared to Cd^{2+}, Mn^{2+}, and Zn^{2+} ions, the composite shows much higher selectivity for Cu^{2+}, including in real mining wastewater conditions, demonstrating its application for selective heavy metal remediation in complex water systems. In addition, using natural mineral resources from North Toraja as a precursor for CAN synthesis provides significant advantages in terms of sustainability, low production costs, and environmental friendliness, making this composite a promising alternative adsorbent for wastewater treatment applications. This finding advances current knowledge about zeolite-biopolymer composite by showing that CAN-based zeolite combined with chitosan can simultaneously provide structural stability, selective adsorption behavior, and high adsorption performance for the removal of Cu^{2+} from industrial wastewater. Further research should focus on regeneration-reuse cycles, continuous flow column adsorption, competitive adsorption in multicomponent systems, and pilot-scale application studies to evaluate long-term operational stability and industrial feasibility of the composite material.

3.9. Acknowledgment

The authors wish to express their gratitude to all parties who have contributed to and supported this research. The authors also wish to thank the Department of Chemistry, Master's Program in Chemistry, Faculty of Mathematics and Natural Sciences, Hasanuddin University, Makassar, Indonesia, for providing research and development laboratories, physical chemistry laboratories, analytical laboratories, and integrated laboratory facilities, as well as technical support during this research.

3.10. CRediT Author Statement

J.B. Matande: Conceptualization, Methodology, Investigation, Resources, Data Curation, Writing, Review and Editing; D.N. Basir: Conceptualization, Methodology, Formal Analysis, Data Curation, Writing Draft Preparation, Visualization, Software, and Project Administration; P. Taba: Conceptualization, Methodology, Formal Analysis, Data Curation, Writing Draft Preparation, Visualization, Software, and Project Administration; S. Fauziah: Validation, Writing, Review and Editing, Data Curation; S. Kasim: Validation, Writing, Review and Editing; and H. Natsir: Validation, Writing, Review and Editing. All authors have reviewed and approved the final version of this manuscript.

3.11. References

[1]. Oladimeji, T. E., Oyedemi, M., Emetere, M. E., Agboola, O., Adeoye, J. B., and Odunlami, O. A., (2024). Review on the impact of heavy metals from industrial wastewater effluent and removal technologies. *Heliyon, 10* (24), e40370. DOI: 10.1016/j.heliyon.2024.e40370.

[2]. Ruzi, I. I., Ishak, A. R., Abdullah, M. A., Zain, N. M. M., Tualeka, A. R., Adriyani, R., Mohamed, R., Edinur, H. A., and Aziz, M. Y., (2024). Heavy metal contamination in Sungai Petani, Malaysia: A wastewater-based epidemiology study. *Journal of Water and Health. 22*(6), 953-966. DOI: 10.2166/wh.2024.241

[3]. Odumbe, E., Murunga, S., and Ndiiri, J., (2023). Heavy Metals in Wastewater Effluent: Causes, Effects, and Removal Technologies. *Trace Metals in the Environment*. IntechOpen. DOI: 10.5772/intechopen.1001452

[4]. Shrestha, R., Ban, S., Devkota, S., Sharma, S., Joshi, R., Tiwari, A. P., Kim, H. Y., Joshi, M. K., (2021). Technological trends in heavy metals removal from industrial wastewater: a review, J. Environ. Chem. Eng, 9 (4), 105688. DOI: 10.1016/j.jece.2021.105688

[5]. Chai, W. S., Cheun, J. Y., Kumar, P. S., Mubashir, M., Majeed, Z., Banat, F., Ho, S., and Show, P. K., (2021). A review on conventional and novel materials towards heavy metal adsorption in wastewater treatment application. *Journal of Cleaner Production*, 296, 126589. DOI: 10.1016/j.jclepro.2021.126589

[6]. Vo, T. T. T., Peng, T. Y., Nguyen, T. H., Bui, T. N. H., Wang, C. S., Lee, W. J., Chen, Y. L., Wu, Y. C., and Lee, I. T., (2024). The crosstalk between copper-induced oxidative stress and cuproptosis: a novel potential anticancer paradigm. *Cell Commun Signal*, *22* (353), 2024. DOI: 10.1186/s12964-024-01726-3

[7]. Genchi, G., Sinicropi, M. S., Lauria, G., Carocci, A., and Catalano, A., (2020).

The Effects of Cadmium Toxicity. *Int. J. Environ. Res. Public Health, 17* (11), 3782. DOI: 10.3390/ijerph17113782

[8]. Zhang, K., Long, M., Dong, W., Li, J., Wang, X., Liu, W., Huang, Q., Ping, Y., Zou, H., Song, R., Liu, G., Ran, D., and Liu, Z., (2024). Cadmium Induces Kidney Iron Deficiency and Chronic Kidney Injury by Interfering with the Iron Metabolism in Rats. *Int J Mol Sci, 25* (2), 763. DOI: 10.3390/ijms25020763.

[9]. Lamas, G. A., Navas-Acien, A., Mark, D. B., and Lee, K. L., (2016). Heavy Metals, Cardiovascular Disease, and the Unexpected Benefits of Chelation Therapy. *J Am Coll Cardiol*, *67* (20), 2411-2418. DOI: 0.1016/j.jacc.2016.02.066

[10]. Kunioka, C. T., Manso, M. C., and Carvalho, M., (2023). Association between Environmental Cadmium Exposure and Osteoporosis Risk in Postmenopausal Women: A Systematic Review and Meta-Analysis. *Int. J. Environ. Res. Public Health*, *20* (1), 485. DOI: 10.3390/ijerph20010485

[11]. Liu, Y., Wang, H., Cui, Y., and Chen, N., (2023). Removal of Copper Ions from Wastewater: A Review. *Int. J. Environ. Res. Public Health, 20* (5), 3885. DOI: 10.3390/ijerph20053885

[12]. Zhang, Y., and Duan, X., (2020). Chemical precipitation of heavy metals from wastewater by using the synthetical magnesium hydroxy carbonate. *Water Sci Technol*, *81* (6), 1130-1136. DOI: 10.2166/wst.2020.208

[13]. Massoud, R., Hadiani, M. R., Hamzehlou, P., and Khosravi-Darani, K., (2019). Bioremediation of heavy metals in food industry: Application of Saccharomyces cerevisiae. *Electronic Journal of Biotechnology*, *37*, 55-60. DOI: 10.1016/j.ejbt.2018.11.003

[14]. Skotta, A., Jmiai, A., Elhaayaoui, W., El-Asri, A., Tamimi, M., Assabbane, A.,

and Issami, S. E., (2023). Suspended matter and heavy metals (Cu and Zn) removal from water by coagulation/flocculation process using a new Bio-flocculant: Lepidium sativum. *Journal of the Taiwan Institute of Chemical Engineers*, *145*, 104792. DOI: 10.1016/j.jtice.2023.104792

[15]. Fadlilah, I., Prasetya, A., and Mulyono, P., (2018). Recovery Ion Hg2+ dari Limbah Cair Industri Penambangan Emas Rakyat dengan Metode Presipitasi Sulfida dan Hidroksida. *Journal Rekayasa Proses, 12* (1), 23. DOI: 10.22146/jrekpros.34496

[16]. Anami, W. R., Maslahat, M., and Arrisujaya, D., (2020). Presipitasi logam berat limbah cair laboratorium menggunakan natrium sulfida dari belerang alam. *Sains Natural*, *10* (2), 61-70. DOI: 10.31938/jsn.v10i2.283

[17]. Lissarrague, M. H. S., Alshehri, S., Alsalhi, A., Lasselle, V. L., and Corral, I. L., (2023). Heavy Metal Removal from Aqueous Effluents by TiO2 and ZnO Nanomaterials. *Adsorption Science & Technology, 2023*, 2728305. DOI: 10.1155/2023/2728305

[18]. Farhan, A., Zulfiqar, M., Samiah, Rashid, E. U., Nawaz, S., Iqbal, H. M. N., Jesionowski, T., Bilal, M., and Zdarta, J., (2023). Removal of Toxic Metals from Water by Nanocomposite through Advanced Remediation Processes and Photocatalytic Oxidation. *Curr Pollution Rep, 9*, 338-358. DOI: 10.1007/s40726-023-00253-y

[19]. Cerrillo-Gonzalez, M. d. M., Villen-Guzman, M., Rodriguez-Maroto, M., and Paz-Garcia, J. M., (2024). Metal Recovery from Wastewater Using Electrodialysis Separation. *Metals*, *14* (1), 38. DOI: 10.3390/met14010038

[20]. Zha, F., Wang, S., Liu, Z., Dai, J., Yue, S., Qi, W., Xue, X., Wang, X., and Zhang, S., (2024). Removal of heavy metals from fly ash using electrodialysis driven by a bioelectrochemical system: a case study of Pb, Mn, Cu and Cd. *Environmental Technology*, *45*(14), 2709–2720. DOI: 10.1080/09593330.2023.2185818

[21]. Birniwa, A. H., Habibu, S., Abdullahi, S. S., Mohammad, R. E. A., Husaini, A., Magaji, H., Al-dhawi, B. N. S., Noor, A., and Jagaba, A. H., (2024). RETRACTED: Membrane technologies for heavy metals removal from water and wastewater: A mini review. *Case Studies in Chemical and Environmental Engineering, 9*, 100538. DOI: 10.1016/j.cscee.2023.100538

[22]. Vallero, D. A., (2024). *Fundamentals of Water Pollution: Quantifying Pollutant Formation, Transport, Transformation, Fate, and Risks. Academic Press*. DOI: 10.1016/C2023-0-50836-5

[23]. Song, J., Heinonen, J., and Sainio, T., (2024). Recovery of ammonium from stormwater by ion exchange: Purifying seepage water in laboratory and pilot scales. *Desalination and Water Treatment, 317*, 100107. DOI: 10.1016/j.dwt.2024.100107

[24]. Chakraborty, R., Asthana, A., Singh, A. K., Jain, B., and Susan, A. B. H., (2022). Adsorption of heavy metal ions by various low-cost adsorbents: a review. *International Journal of Environmental Analytical Chemistry, 102* (2), 342-379. DOI: 10.1080/03067319.2020.1722811

[25]. Amin, I. I., Wahab, A. W., Mukti, R. R., and Taba, P., (2023). Synthesis and characterization of zeolite type ANA and CAN framework by hydrothermal method of Mesawa natural plagioclase feldspar. *Applied Nanoscience*, *13*, 5389-5398. DOI: 10.1007/s13204-022-02756-4

[26]. Mancinelli. M., Precisvalle, N., Ardit, M., Beltrami, G., Gigli, L., Catizzone, E., Migliori, M., Giodani, G., and Martucci, A., (2023). Thermal stability of templated ZSM-5 zeolites: An in-situ synchrotron X-ray powder diffraction study. *Microporous and Mesoporous Materials*, *362*, 112777. DOI: 10.1016/j.micromeso.2023.112777

[27]. Siora, I., Andriyko, L., Gerashchenko, I., Borysenko, M., Paklov, E., Oranska,

O., Lytvnenko, Y., Tysba, M., Odynchenko, R., and Goncharuk, O., (2025). Comparative study of the structural characteristics and adsorption capacity of natural and synthetic zeolites. *Microporous and Mesoporous Materials, 397*, 113778. DOI: 10.1016/j.micromeso.2025.113778

[28]. Yuna, Z., (2016). Review of the Natural, Modified, and Synthetic Zeolites for Heavy Metals Removal from Wastewater. *Environmental Engineering Science, 33* (7), 443-454. DOI: 10.1089/ees.2015.0166

[29]. Hong, M., Yu, L., Wang, Y., Zhang, J., Chen, Z., Dong, L., Zan, Q., and Li, R., (2019). Heavy metal adsorption with zeolites: The role of hierarchical pore architecture. *Chemical Engineering Journal, 359*, 363-372. DOI: 10.1016/j.cej.2018.11.087

[30]. Mahmodi, G., Zarrintaj, P., Taghizadeh, A., Taghizadeh, M., Manouchehri, S., Dangwal, S., Ronte A., Ganjali, M.R., Ramsey, J. D., Kim, S-K., and Saeb, M. R., (2020). From microporous to mesoporous mineral frameworks: An alliance between zeolite and chitosan. *Carbohydrate Research*, *489*, 107930. DOI: 10.1016/j.carres.2020.107930

[31]. Taba, P., Fauziah, St., Natzir, H., Soekamto, N. H., Sarungallo, R. S., Nahru, N. W., Astuti, Y., and Amin, I. I., (2025). Synthesis and characterization of zeolite obtained from Toraja natural montmorillonite. *Journal of the Serbian Chemical Society, 90* (6), 753-766. DOI: 10.2298/JSC241012015T

[32]. Challab, M. K., Chaichi, M. J., Khathi, M. K., Nazari, O., and Ghasemi, S., (2025). Adsorption of Cd(II) and Fe(II) Ions by Inorganic Nanocomposite (CuO/ZnO) from Aqueous Solutions. *Indonesia Journal of Chemistry*, *25* (3), 892-904. DOI: 10.22146/ijc.104802

[33]. Raji, Z., Karim, A., Karam, A., & Khalloufi, S. (2023). Adsorption of heavy metals: Mechanisms, kinetics, and applications of various adsorbents in wastewater remediation-A review. *Waste*, 1 (3): 775–805. DOI:

10.3390/waste1030046

[34]. Marhoon, A. A., Hasbullah, S. A., Asikin-Mijan, N., & Wan Mokhtar, W. N. A., (2024). Adsorption of metal porphyrins using chitosan/zeolite-X composite as an efficient demetallization agent for crude oil: Isotherm, kinetic, and thermodynamic studies. *International Journal of Biological Macromolecules*, *274*, 133358. DOI: 10.1016/j.ijbiomac.2024.133358

[35]. Sabbagh, N., Tahvildari, K., & Sharif, A. A. M. (2021). Application of chitosan-alginate bio composite for adsorption of malathion from wastewater: Characterization and response surface methodology. *Journal of Contaminant Hydrology*, *242*, 103868. DOI: 10.1016/j.jconhyd.2021.103868

[36]. Phuoc, N. M., Thien, L. T., Phuong, N. T. T., Duoang, N. T. H., Dung, N. V., and Lang, N. Q., (2024). Novel chitosan-zeolite X composite beads prepared by phase-inversion method for CO_2 adsorptive capture. *Chemosphere*, *352*, 141327.
DOI: 10.1016/j.chemosphere.2024.141327

[37]. Araujo, L. G. d., Medeiros, V. L., Guarnieri, G. d. P., Silva, D. A. d., Watanabe, T., Marumo, J. T., and Nery, J. G., (2023). An adsorption agent based on chitosan–zeolite composite: environmental and radioactive liquid waste remediation. *Environmental Science: Advances, 2* (3), 484-494.
DOI: 10.1039/D2VA00148A

[38]. Hidayat, E., Yoshino, T., Yonemura, S., Mitoma, Y., and Harada, H., (2023). A Carbonized Zeolite/Chitosan Composite as an Adsorbent for Copper (II) and Chromium (VI) Removal from Water. *Materials*, *16* (6), 2532.
DOI: 10.3390/ma16062532

[39]. Şanlı, G.T., and Demirhan, E., (2025). Preparation and characterization of chitosan/zeolite composite for Reactive Orange 122 dye removal from aqueous media: isotherm and kinetic studies. *Biomass Conv. Bioref, 15*, 3653-3662.
DOI: 10.1007/s13399-024-05284-z

[40]. Kołodyńska, D., Hałas, P., Franus, M., & Hubicki, Z. (2017). Zeolite properties improvement by chitosan modification—Sorption studies. *Journal of Industrial and Engineering Chemistry*, *52*, 187–196. DOI: 10.1016/j.jiec.2017.03.041

[41]. Gao, Y., Ru, Y., & Wang, J. (2018). Preparation and Characterization of Chitosan–Zeolite Molecular Sieve Composite for Ammonia and Nitrogen Removal. *Journal of Bioactive and Compatible Polymers*, *33*(6), 591–605. DOI: 10.1177/0963693518027005O2

[42]. Hidayat, E., Yoshino, T., Yonemura, S., Mitoma, Y., & Harada, H. (2022). Synthesis, adsorption isotherm and kinetic study of alkaline treated Zeolite/Chitosan/Fe^{3+} composite for nitrate removal from aqueous solution anion and dye effects. *Gels*, 8 (12): 782. DOI: 10.3390/gels8120782

[43]. Shi, Y., Wang, X., Feng, C., Chen, W., & Yang, S. (2024). Adsorption properties of natural zeolite supported by chitosan on Cd (II) in micropolluted irrigation water. *ACS Omega*, 9 (1): 573–584. DOI: 10.1021/acsomega.3c06041

[44]. Manu, G. P., Narh, D., Asimeng, B., Kwakye, N., Abusuapa, B. A., Appuing, D., Nyankson, E., & Efavi, J. K. (2025). Characterization of Chitosan/ Zeolite drug delivery composite and curcumin release kinetics in a simulated pH environment. *Scientific African*, *28* (02668). DOI: 10.1016/j.sciaf.2025.e02668

[45]. Kumar, S., Prasad, K., Gil, J. M., Sobral, A. J. F. N., & Koh, J. (2018). Mesoporous zeolite-chitosan composite for enhanced capture and catalytic activity in chemical fixation of CO_2. *Carbohydrate Polymers*, 198: 401–406. DOI: 10.1016/j.carbpol.2018.06.104

[46]. Chen, H., Zhang, Y. J., He, P. Y., Li, C. J., & Liu, L. C. (2020). Novel activated carbon route to low-cost geopolymer based porous composite with high mechanical resistance and enhanced CO_2 capacity. *Microporous and*

Mesoporous Materials, 305 (110282). DOI: 10.1016/j.micromeso.2020.110282

[47]. Saragi, I. R., Khatrin, I., Susilawati, S., Amaturrahim, S. A., Simanjuntak, C., & Hamid, M. (2026). Chitosan/NaY zeolite composite: Porous organic-inorganic hybrid material for efficient adsorption of dyes from aqueous solution. *Inorganic Chemistry Communications*, 116696

[48]. Alehosseini, E., Tabarestani, H. S., Kharazmi, M. S., & Jafari, S. M. (2022). Physicochemical, thermal, and morphological properties of chitosan nanoparticles produced by ionic gelation. *Foods*, 11 (23): 3841. DOI: 10.3390/foods11233841

[49]. Foong, S. Y., Liew, R. K., Yek, P. N. Y., Laing, C. D., Kasan, N. A., Kang, K., Alomairy, S., & Lam, S. S. (2026). Microwave-assisted valorization of black soldier fly pupal and shrimp shells into chitin and chitosan: A rapid biopolymer recovery approach. *International Journal of Biological Macromolecules*, 359 (151644). DOI: 10.1016/j.ijbiomac.2026.151644

[50]. Suhaimi, A., Jawad, A. H., Yusoff, M. Z. M., Wilson, L. D., & ALOthman, Z. A. (2025). Design of composite chitosan/algae/zeolite by freeze or air-drying: A comparative adsorbent analysis for optimized removal of brilliant green dye. *International Journal of Biological Macromolecules*, 288 (138650). DOI: 10.1016/j.ijbiomac.2025.138650

[51]. Okwuenu, P. C., Onosakponome, I., Oparaji, E. H., & Isoje, A. O. (2025). Characterization of chitin and chitosan from shells of water snail (*Pila ampullacea*) using Fourier transform infrared spectroscopy (FTIR). *International Journal of Biological Macromolecules*, 333 (149012). DOI: 10.1016/j.ijbiomac.2025.149012

[52]. Rajan, D. K., Rajarajeswaran, J., Revathi, N., Zhang, S., Mohan, K., & Ganesan, A. R. (2026). Critical insights into coleopteran insect side-streams derived chitin and chitosan: Extraction chemistry, structural features and

multifunctional applications. *Carbohydrate Polymers*, 378 (124958). DOI: 10.1016/j.carbpol.2026.124958

[53]. França, A. M. D. M., Sousa, F. W., Loiola, A. R., Luna, F. M. T. D., Vidal, C. B., & Nascimento, R. F. D. (2021). Study of Cu^{2+}, Ni^{2+}, and Zn^{2+} competitive adsorption on synthetic zeolite: An experimental and theoretical approach. *Desalination and Water Treatment*, 227, 263–277. DOI: 10.5004/dwt.2021.27255

[54]. Meng, Y., Chen, D., Sun, Y., Jiao, D., Zeng, D., & Liu, Z. (2015). Adsorption of Cu^{2+} ions using chitosan-modified magnetic Mn ferrite nanoparticles synthesized by microwave-assisted hydrothermal method. *Applied Surface Science*. 324: 745-750. DOI: 10.1016/j.apsusc.2014.11.028

[55]. Alabi, A. H., Oladele, E. O., Adeleke, A. J. O., Oni, F. C., & Olanrewaju, C. A. (2020). Equilibrium, kinetic and thermodynamic studies of biosorption of methylene blue on goethite modified baobab fruit pod (*Adansonia digitata L.*). *Journal of Applied Sciences and Environmental Management*, 24 (7): 1229–1243. DOI: 10.4314/jasem.v24i7.16

[56]. Wang, J., Guo, X., (2020). Adsorption isotherm models: Classification, physical meaning, application and solving method. *Chemosphere*, 258: 1-74. DOI: 10.1016/j.chemosphere.2020.127279

[57]. Moktar, A., Daaou, M., Bendraoua, A., & Morsli, A. (2022). Study of Cu^{2+}, Zn^{2+} and Mn^{2+} ions adsorption using asphaltenes-chitosan composite beads. *Materials Today Communications*, 33 (104928). DOI: 10.1016/j.mtcomm.2022.104928

[58]. Hu, C., Zheng, Z., Huang, M., Yang, F., Wu, X., & Zhang, A. (2023). Adsorption characterization of Cu (II) and Cd (II) by a magnetite–chitosan composite: Kinetic, thermodynamic and equilibrium studies. *Polymers*, 15 (12): 2710-2721. DOI: 10.3390/polym15122710

[59]. Priyadi, Iskandar, Suwardi, Mukti, R.R., (2016). Characteristics of heavy metals adsorption Cu, Pb and Cd using synthetics Zeolite ZSM-5. *J. Trop. Soils,* 20 (2): 77-83. DOI: 10.5400/jts.2015.v20i2.77-83.

[60]. Uddin, M. T., Rukanuzzaman, M., & Islam, M. A. (2022). Enhanced adsorption performance of activated carbon prepared from peanut shell for the adsorption of dyes from aqueous solution. *Desalination and Water Treatment*. 280: 60–75. DOI: 10.5004/dwt.2022.28961

[61]. Anggriani, U.M., Hasan, A., and Purnamasari, I., (2021). Adsorption kinetics of activated carbon in reducing the concentration of copper (Cu) and lead (Pb) metals. *Journal of Kinetics*, 2 (12): 29-37.

[62]. Alves, D. C. d. S., Healy, B., Pinto, L. A. de A., Cadaval, T. R. S., Jr., & Breslin, C. B. (2021). Perkembangan terbaru dalam adsorben berbasis chitosan untuk penghilangan pencemar dari lingkungan akuatik. *Molecules*. 26 (3): 594. DOI: 10.3390/molecules26030594

[63]. Rukhsar, A., Iqbal, Z.F., Khan, M.S., et al. (2024). Chitosan-based adsorbents and catalysts for removal of toxic pollutants from water and wastewater. *Topics in Catalysis,* 68: 893–915. DOI: 10.1007/s11244-024-03012-7

[64]. Zhang, Y., Zhao, M., Cheng, Q., Wang, C., Li, H., Han, X., Fan, Z., Su, G., Pan, D., & Li, Z. (2021). Research progress of adsorption and removal of heavy metals by chitosan and its derivatives: A review. *Chemosphere*, 279, 130927. DOI: 10.1016/j.chemosphere.2021.130927

[65]. Detho, A., Memon, A.H., Almohana, A.I., et al. (2023). Sorption kinetics, isotherm studies and mechanism of removal of organic and inorganic pollutants by renewable biomineral. *Water, Air, & Soil Pollution*, 234 (22). DOI: 10.1007/s11270-023-06578-9

[66]. Liu, X., Zhao, X., Liu, Y., & Zhang, T. (2022). *Review on preparation and adsorption properties of chitosan and chitosan composite. Polymer Bulletin.* 79: 2633–2665. DOI: 10.1007/s00289-021-03756-4

[67]. Amrutha, Jeppu, G., Girish, C. R., Prabhu, B., & Mayer, K. (2023). Multi-component adsorption isotherms: Review and modeling studies. *Environmental Processes*, 10 (38). DOI: 10.1007/s40710-023-00631-0

[68]. Fan, X., Liu, H., Anang, E., & Ren, D. (2021). Effects of electronegativity and hydration energy on the selective adsorption of heavy metal ions by synthetic NaX zeolite. *Materials*, 14 (15): 4066. DOI: 10.3390/ma14154066

[69]. BPS of Southeast Sulawesi Province. (2022). Southeast Sulawesi Province in Figures 2022. First Edition. Kendari: BPS of Southeast Sulawesi Province.

[70]. Purnama, M. F., Suprihanto, A., & Hadiyanto, H. (2024). Assessment of aquatic environmental quality based on bioindicators (gastropods) in areas affected by nickel mining in Pomalaa District, Southeast Sulawesi. *Journal of the Indonesian Engineering*, 2 (6): 359-370. DOI: 10.14710/jpii.2024.24930

[71]. Amelia, F. R., Effendi, H., Kurniawan, B., Andrianto, C., & Ahmady, T. (2025). Analysis of water quality and nickel mining waste in the Pesouha River, Southeast Sulawesi. *Journal of Sustainable Environmental Management*, 9 (1): 1-14. DOI: 10.36813/jplb.9.1.1-14

[72]. Hasria, H., Usman, I., Saeri, K., Nasaruddin, N., Septiana, S., Rais, M., Harisma, H., & Musrajab, S. (2026). Analysis of content, source and impact of heavy metals in Sombori Island, Central Sulawesi, Indonesia. *Journal of Geoscience, Engineering, Environment, and Technology*, 11 (1). DOI: 10.25299/jgeet.2026.11.1.23856

[73]. Susiana, C. A., Rusdiarso, B., and Mudasir, M., 2024. Enhanced Capacity and Easily Separable Adsorbent of Dithizone-immobilized Magnetite Zeolite for

Pb(II) Adsorption. *Indonesian Journal of Chemistry*, *24* (4), 1058-1070. https://doi.org/10.22146/ijc.90914

[74]. Ankrah, A. F., Tokay, B., and Snape, C. E., 2022. Heavy Metal Removal from Aqueous Solutions Using Fly-Ash Derived Zeolite NaP1. *Internasional Journal of Environmental Research*, *16* (17).https://doi.org/10.1007/s41742-022-00395-9

[75]. Küçük, M. E., Makarava, I., Kinnarinen, T., and Häkkinen, A., 2023. Simultaneous adsorption of Cu(II), Zn(II), Cd(II) and Pb(II) from synthetic wastewater using NaP and LTA zeolites prepared from biomass fly ash. *Heliyon*, *9* (10), e20253. 10.1016/j.heliyon.2023.e20253

[76]. Xiong, Q., and Zhang, F., 2022. Study on the Performance of Composite Adsorption of Cu2+ by Chitosan/ß-Cyclodextrin Cross-Linked Zeolite. *Sustainability*, *14* (4), 2106. https://doi.org/10.3390/su14042106

FIGURE CAPTIONS

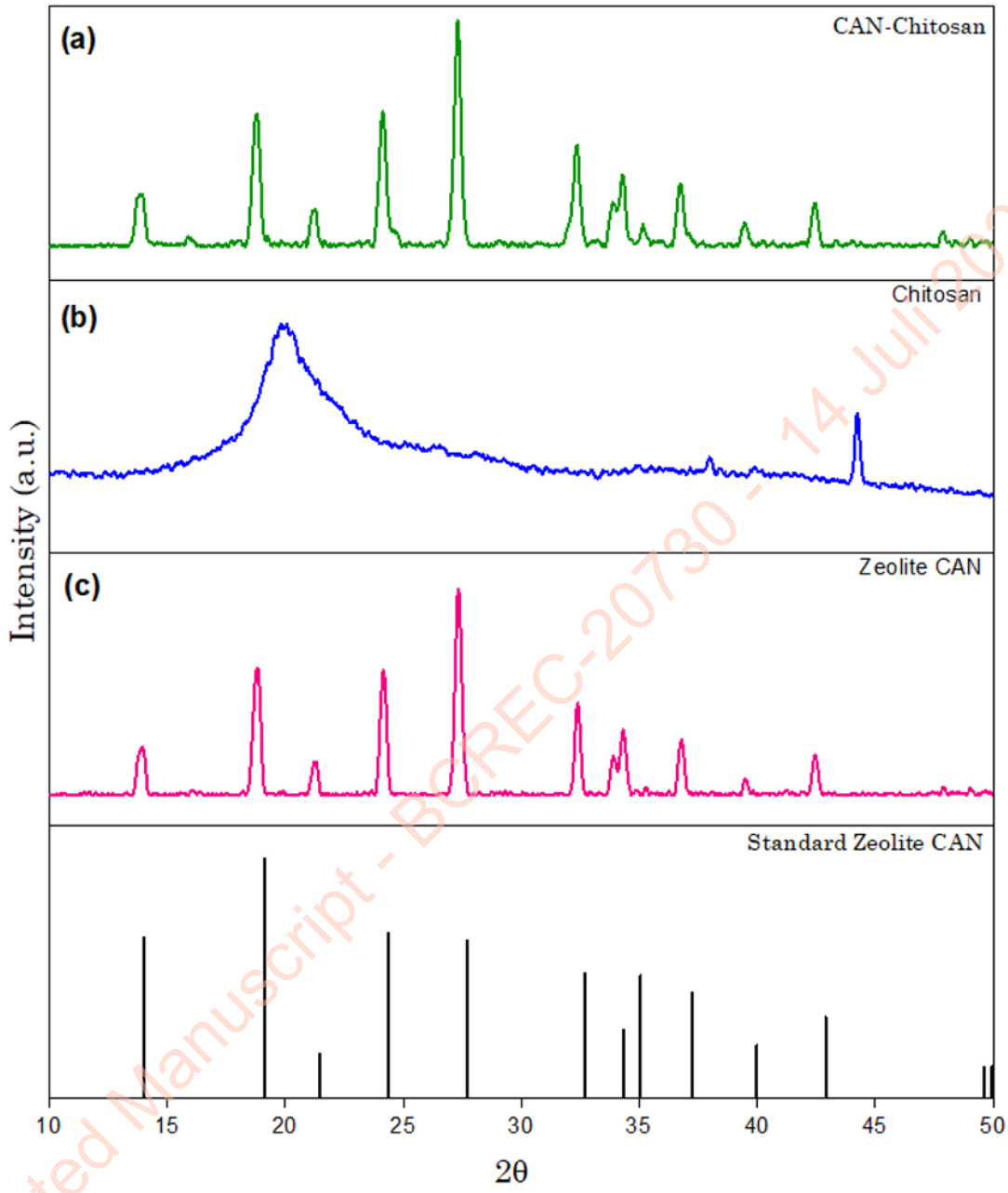

Figure 1. XRD patterns for chitosan, CAN, and CAN-Chitosan

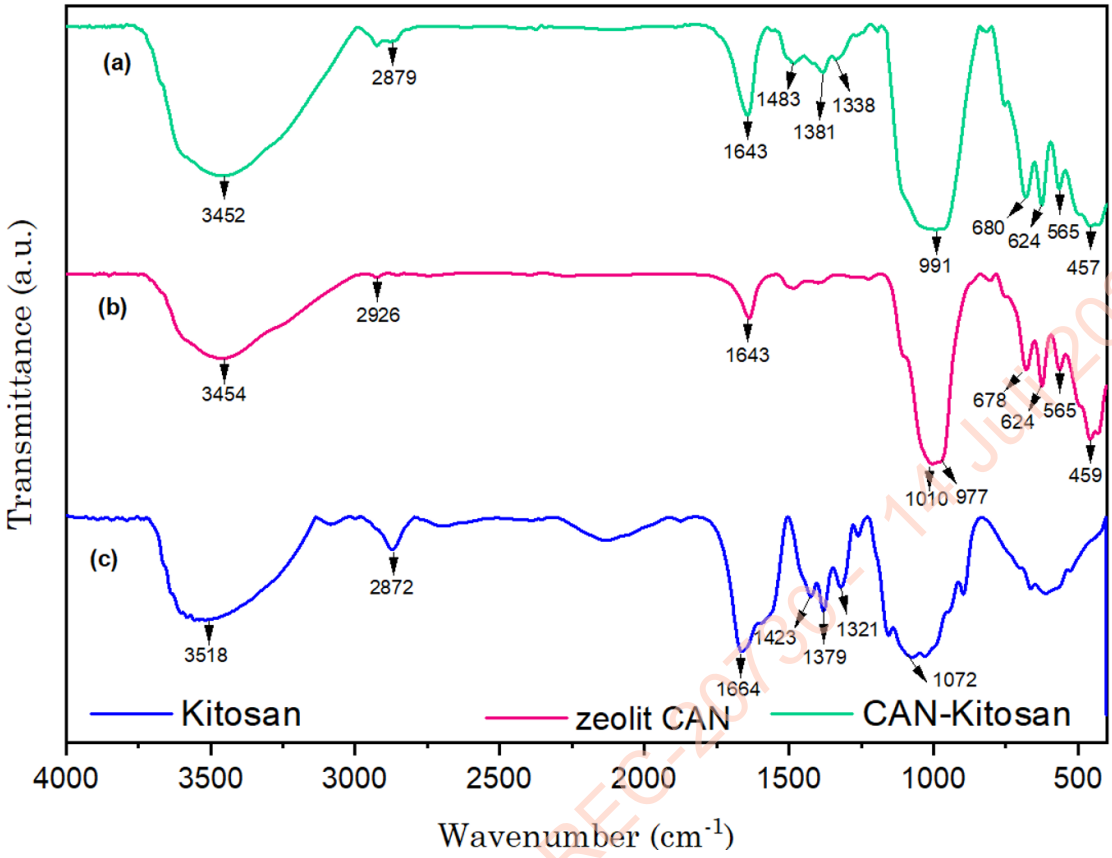

Figure 2. FTIR spectra of chitosan, CAN, and CAN-Chitosan

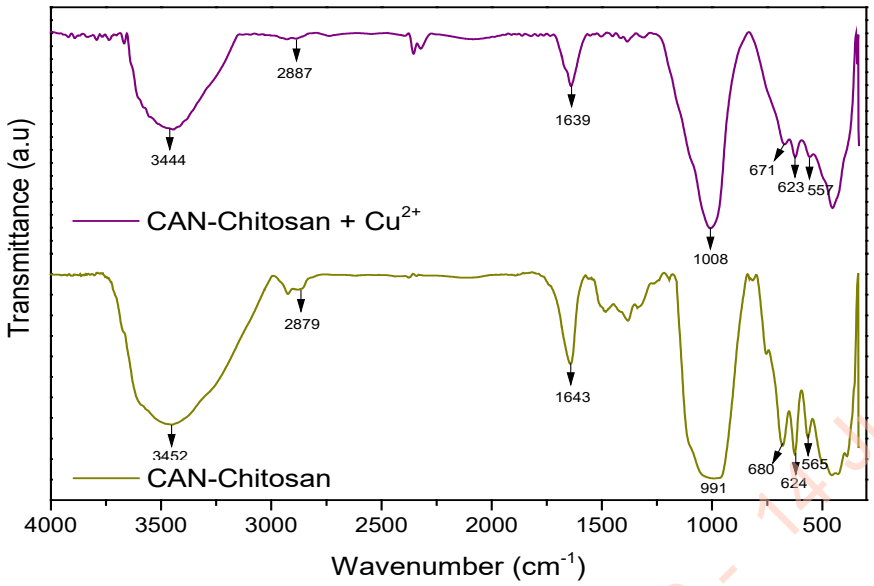

Figure 3. FTIR spectra of the CAN-chitosan composite before and after Cu^{2+} adsorption

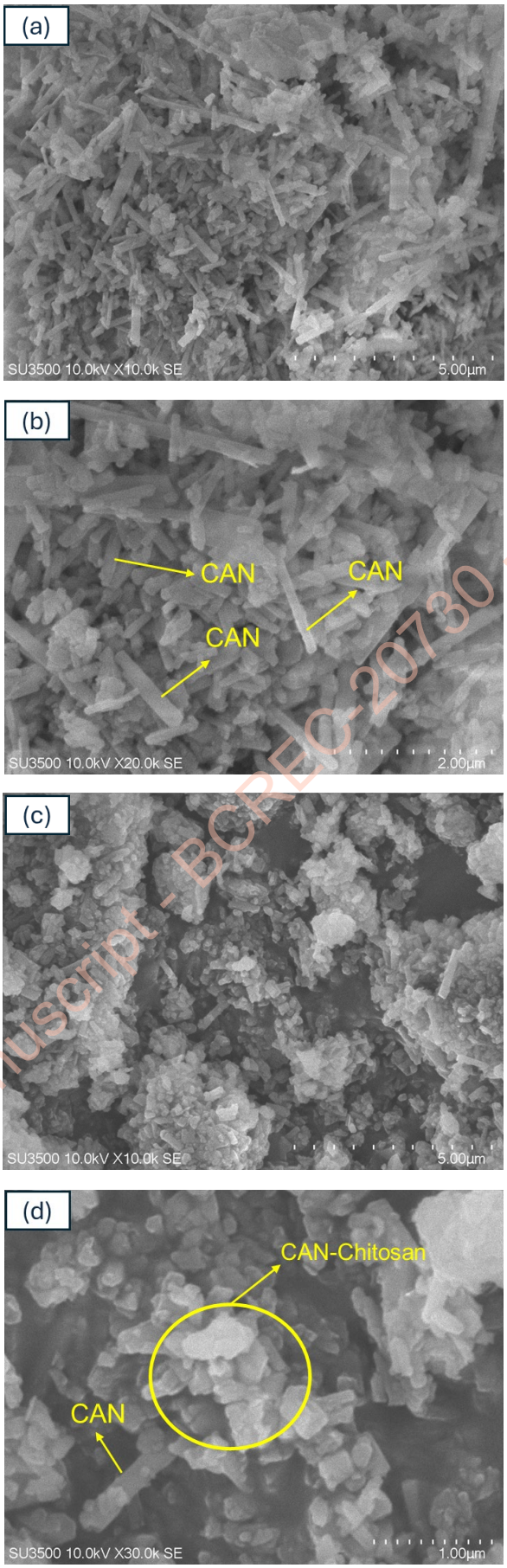

Figure 4. SEM images of (a,b) CAN and (c,d) CAN-Chitosan

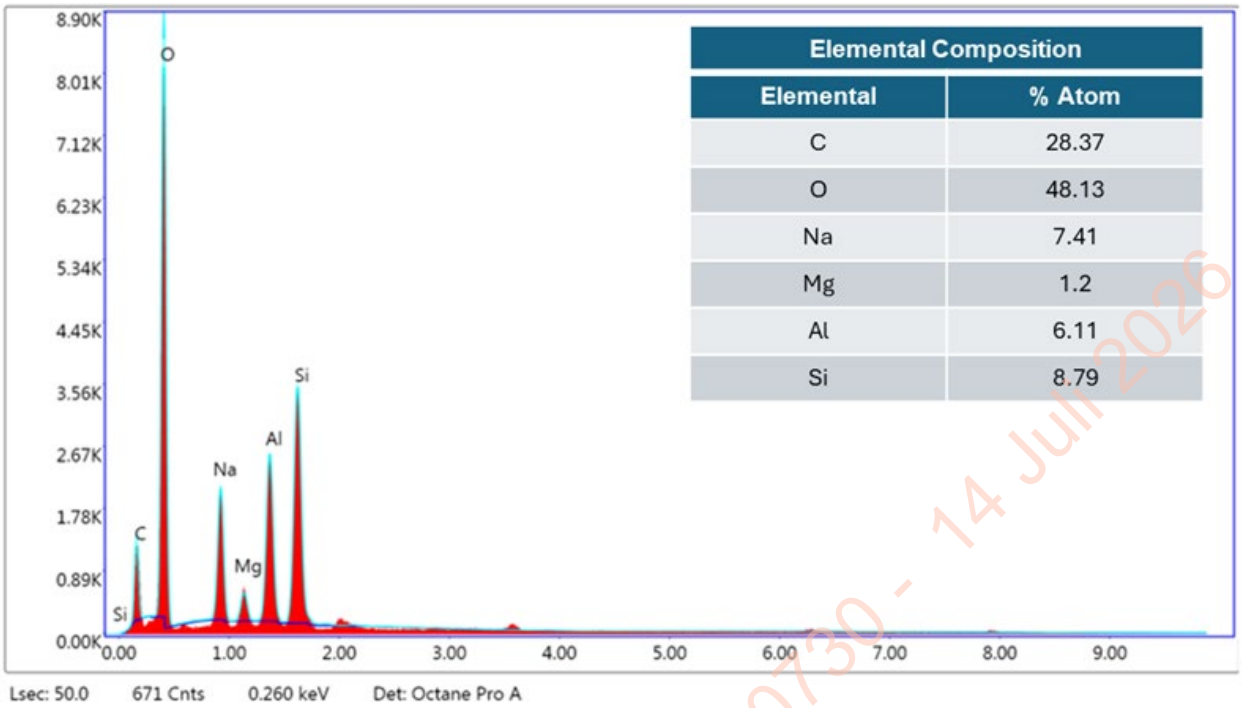

Elemental Composition	
Elemental	% Atom
C	28.37
O	48.13
Na	7.41
Mg	1.2
Al	6.11
Si	8.79

Figure 5. EDS spectrum of the CAN-Chitosan zeolite composite sample

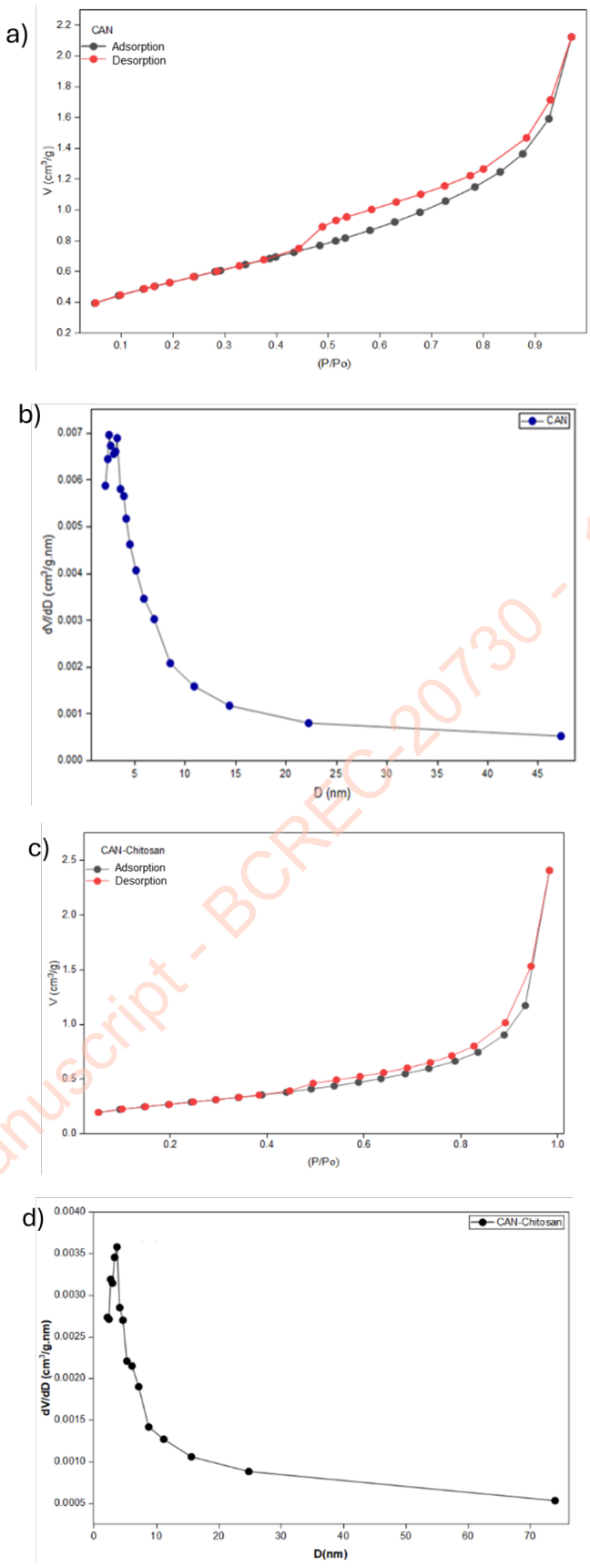

Figure 6. N_2 adsorption-desorption and pore size distribution of: CAN (a, b); CAN-chitosan composite (c, d)

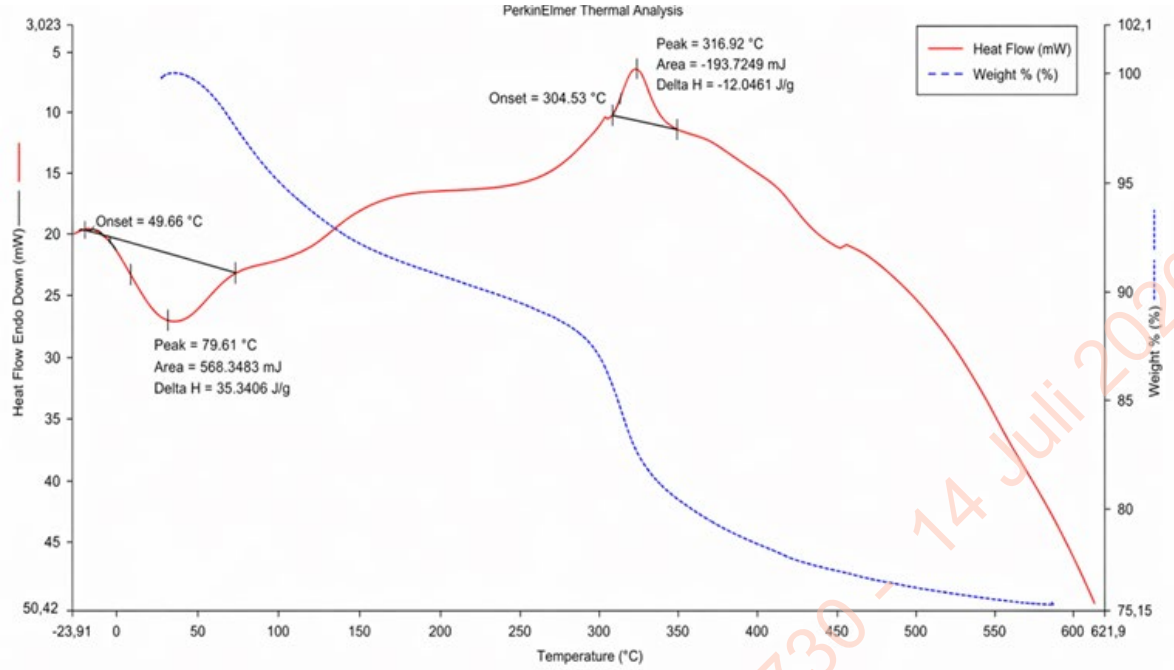

Figure 7. Results of TGA-DSC analysis

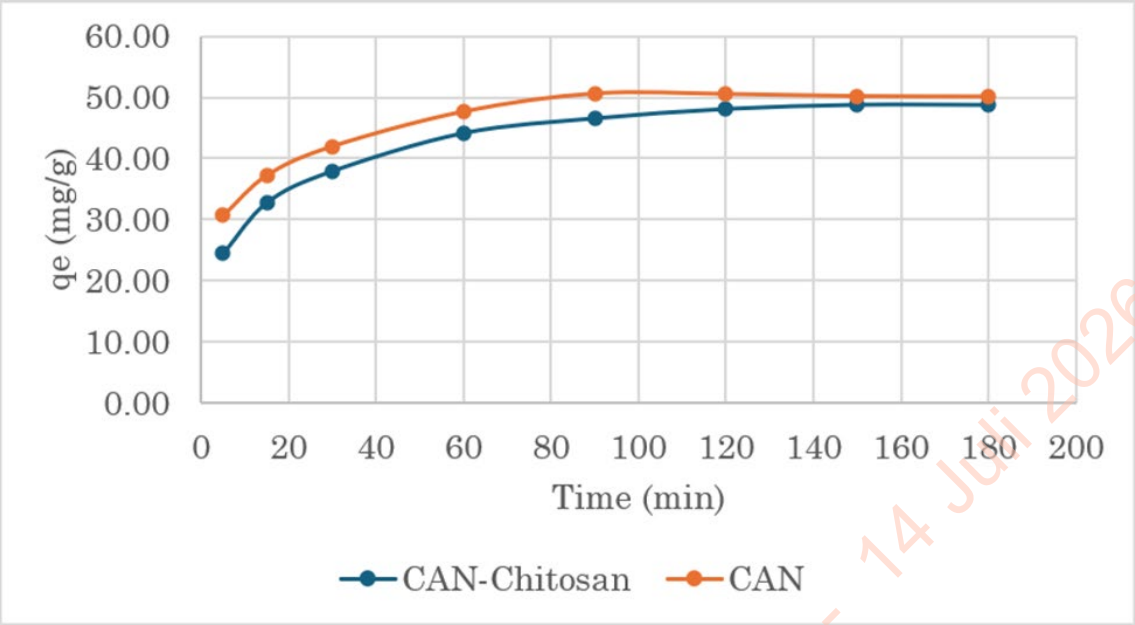

Figure 8. Graph of the relationship between adsorption time and the amount of Cu^{2+} ions adsorbed by CAN-Chitosan zeolite and CAN

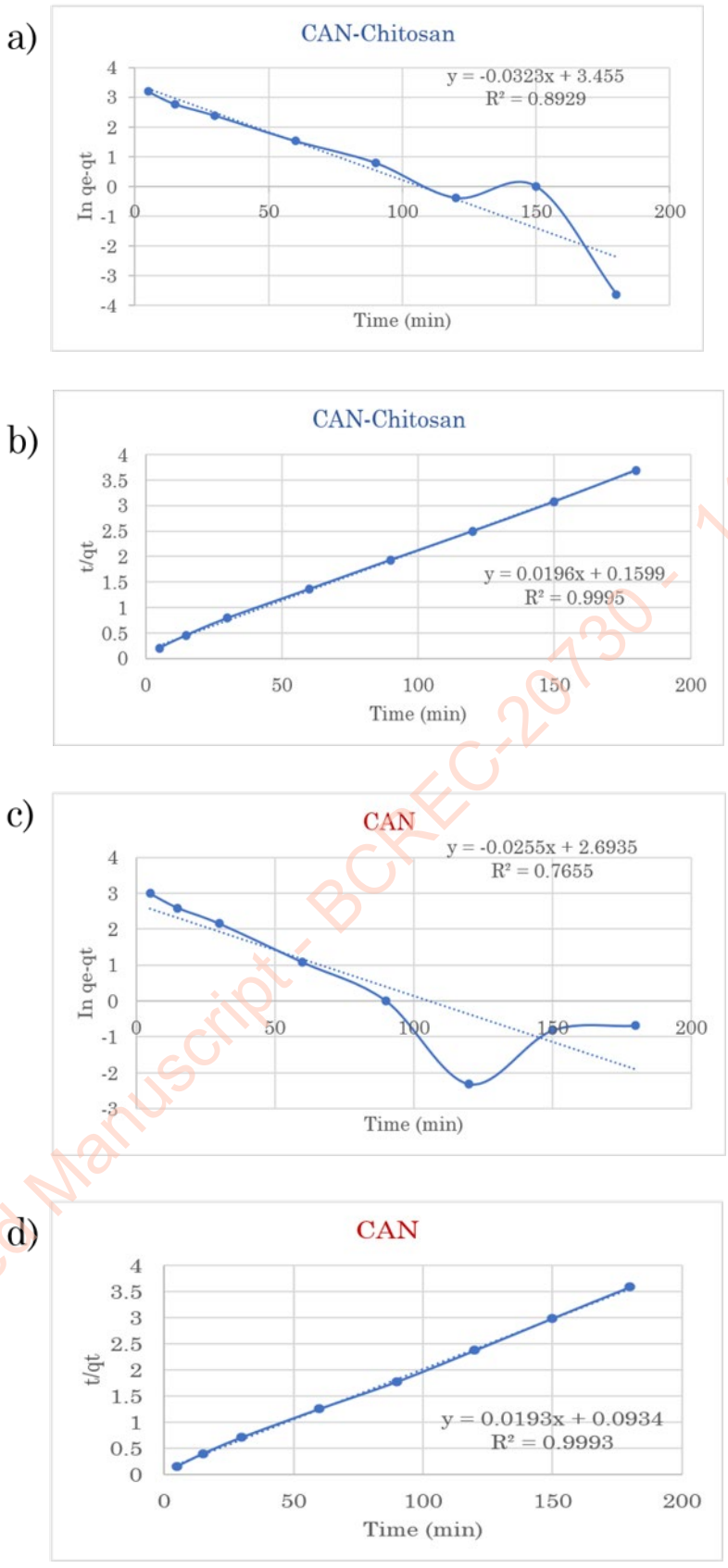

Figure 9. Adsorption kinetics: pseudo first order (a), pseudo second order (b) of Cu^{2+} metal ions by CAN-Chitosan, pseudo first order (c), pseudo second order (d) of Cu^{2+} metal ions by CAN

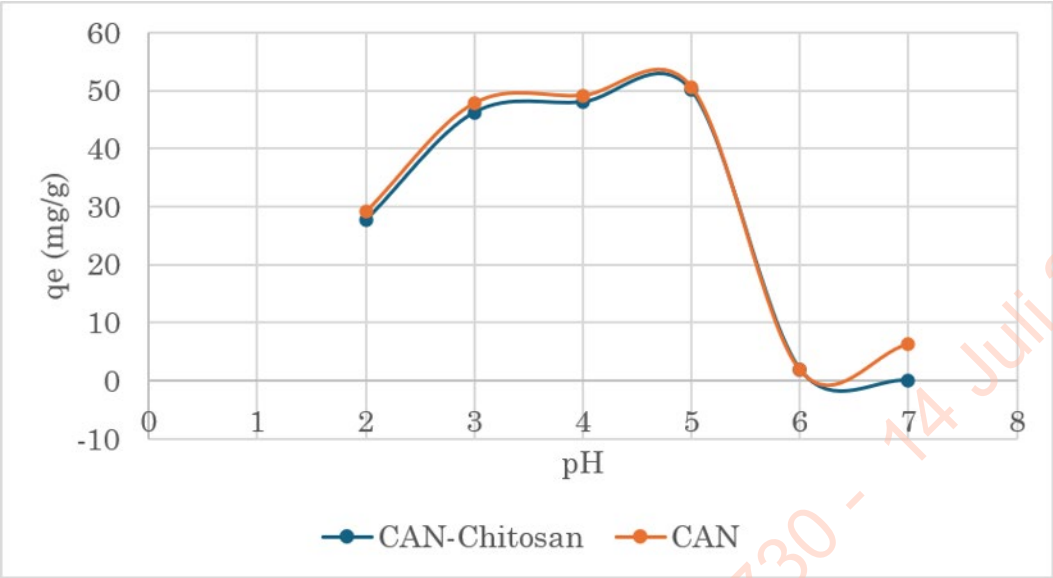

Figure 10. The relationship between the solution pH and the amount of Cu^{2+} ions adsorbed by CAN-chitosan zeolite and CAN

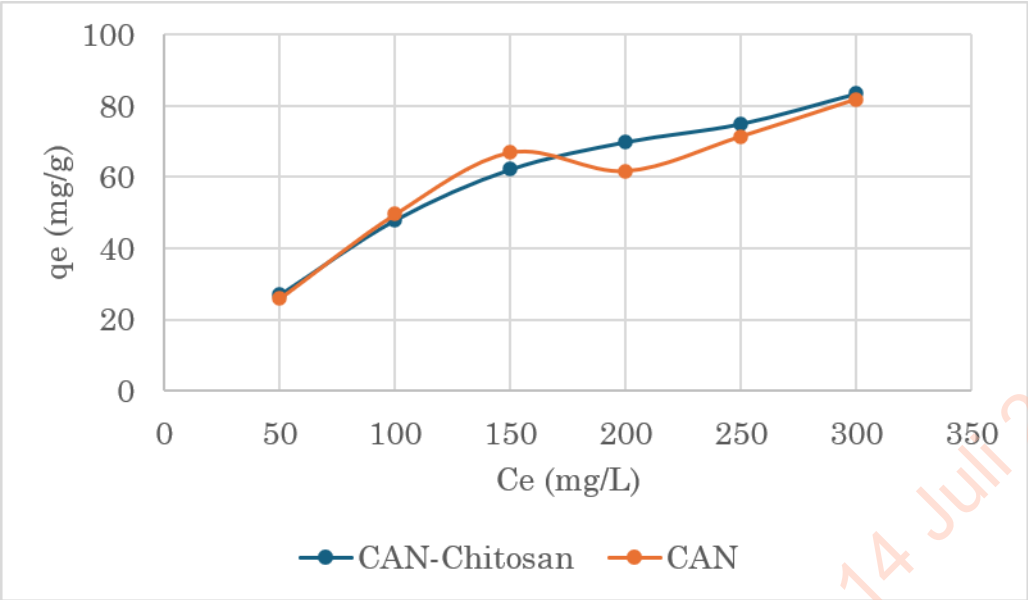

Figure 11. Graph showing the relationship between the initial solution concentration and the amount of Cu^{2+} ions adsorbed by CAN-Chitosan zeolite and CAN

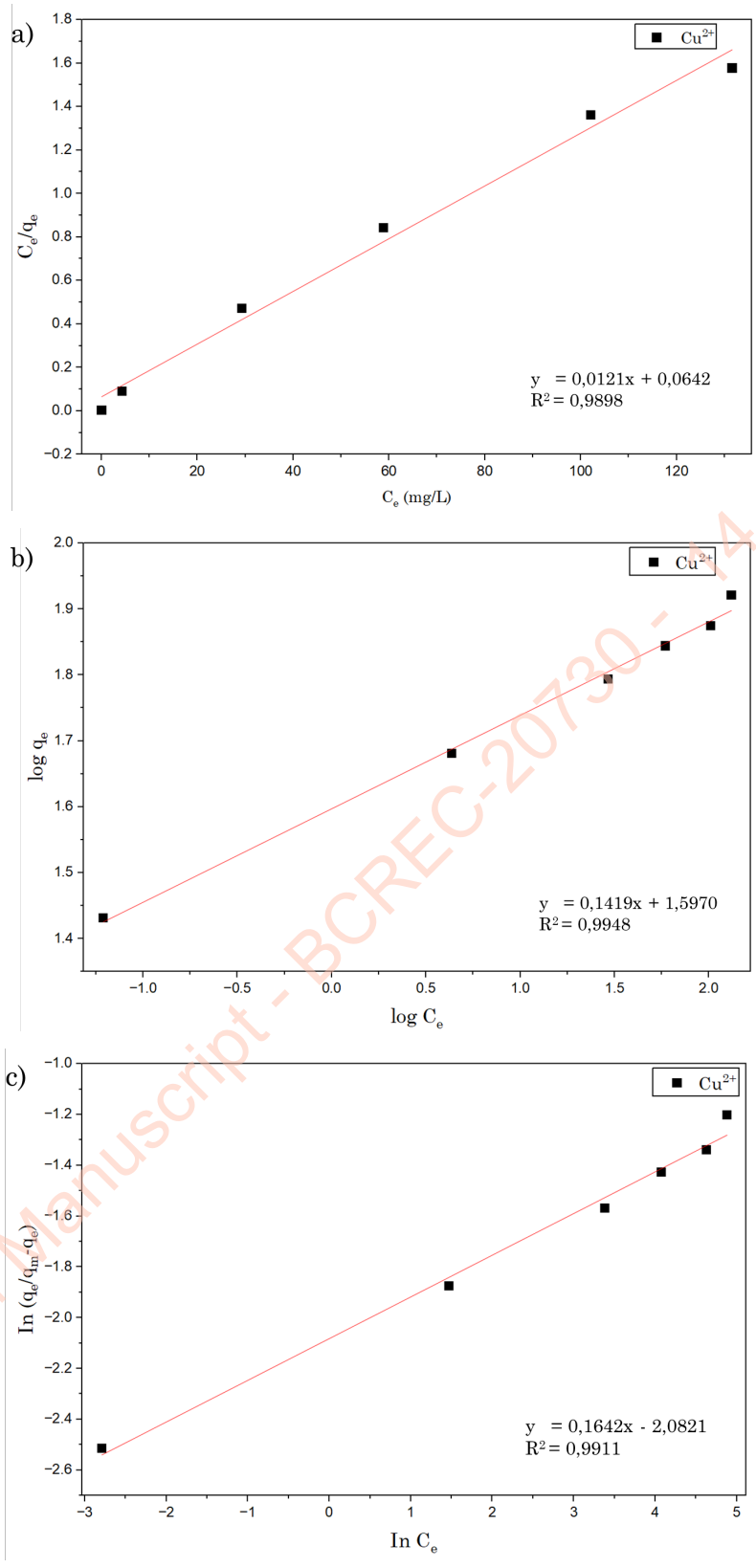

Figure 12. Linear adsorption isotherm graphs: a) Langmuir, b) Freundlich, and c) Sips for Cu^{2+} ion adsorption by CAN-Chitosan

a)

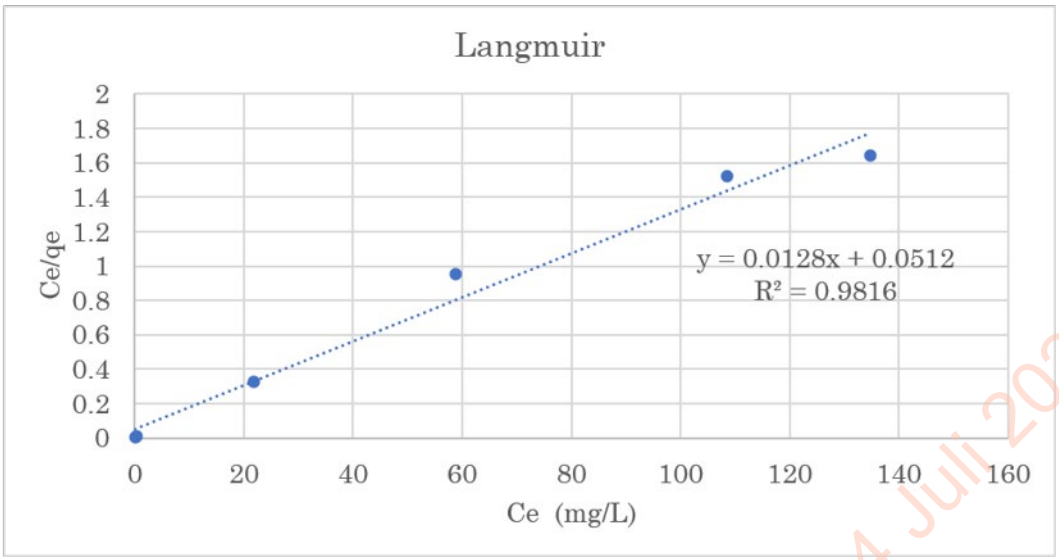

b)

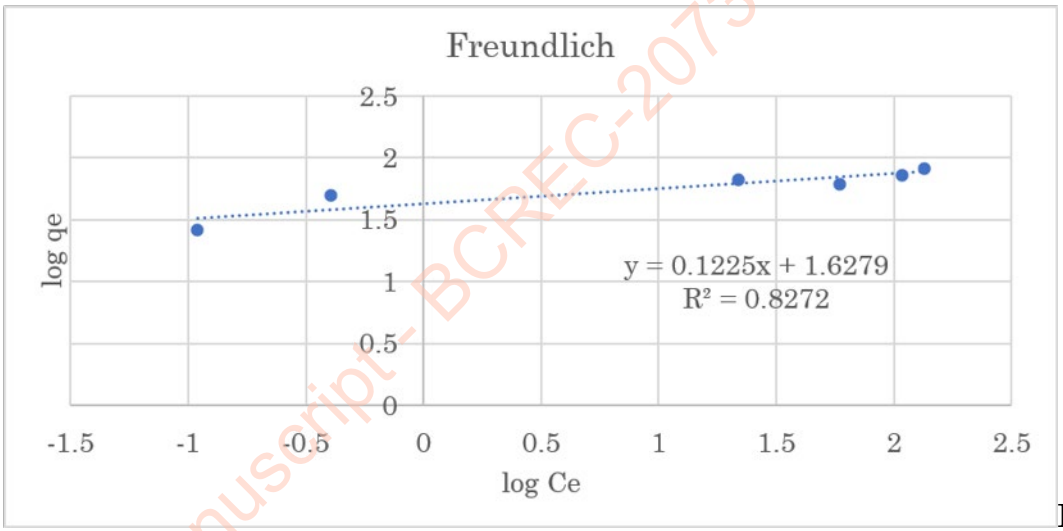

Fig

Figure 13. Linear adsorption isotherm graphs: a) Langmuir and b) Freundlich for Cu^{2+} ion adsorption by CAN

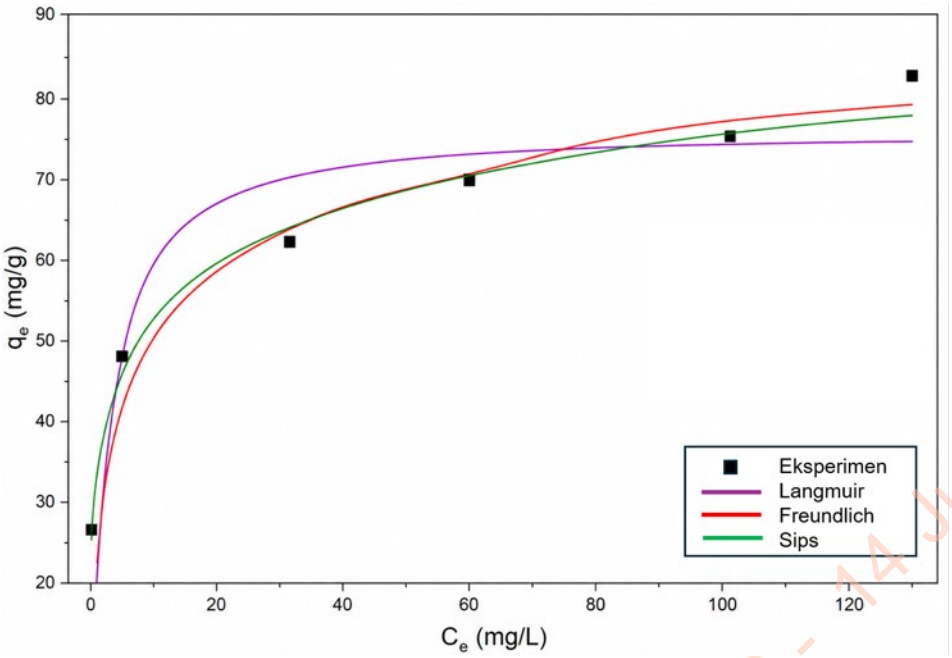

Figure 14. Isotherm graph of non-linear Langmuir, Freundlich, and Sips adsorption for Cu^{2+} ion adsorption by CAN-Chitosan zeolite

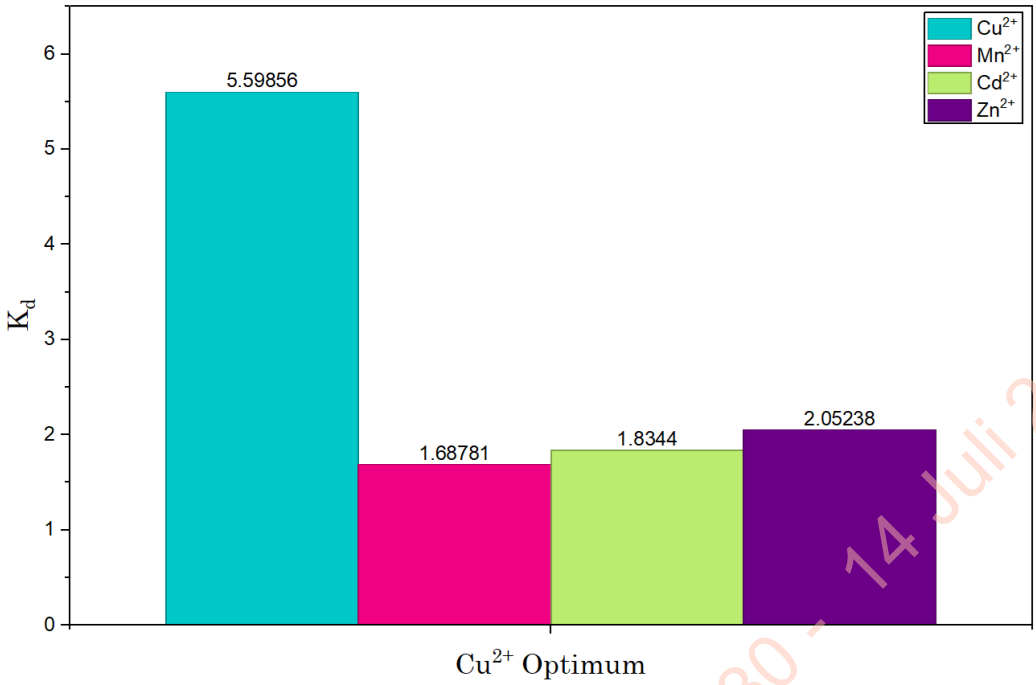

Figure 15. Metal ion adsorption selectivity in a multi-metal system

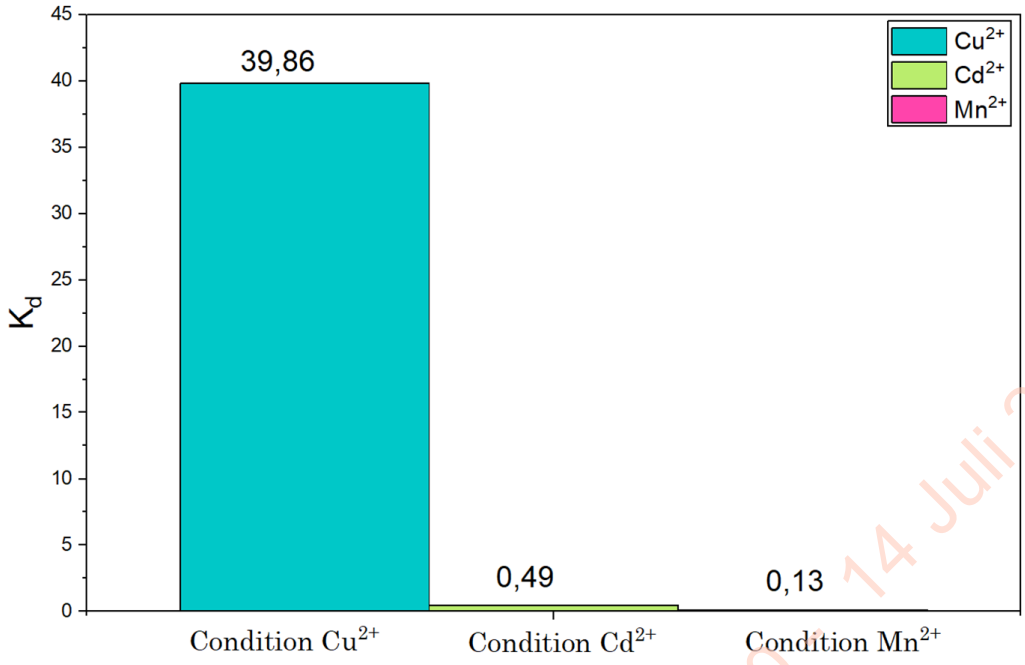

Figure 16. Application of CAN–Chitosan zeolite adsorbent on mining industry wastewater in Southeast Sulawesi

TABLE CAPTIONS

Table 1. The adsorption of Cu^{2+} ions variations

Parameter	**Range**
Contact time (min)	5, 15, 30, 60, 90, 120, 150, 180
Solution pH	2, 3, 4, 5, 6, 7
Initial Cu^{2+} concentration (mg/L)	50, 100, 150, 200, 250, 300

Table 2. Surface area, pore volume, and pore diameter of CANand CAN-Chitosan samples

Sample	BET Surface Area (m^2/g)	Total Pore Volume (adsorption) at p/p0 (cm^3/g)	BJH Adsorption Median Pore Diameter (nm)
CAN	43,0278	0,07363	10,54905
CAN-Chitosan	22,1217	0,08354	28,48086

Table 3. Regression value of pseudo-first-order and scond-order kinetic models

Adsorbent	Pseudo First Order			Pseudo Second Order			q_e experiment ($mg.g^{-1}$)
	K_1 (min^{-1})	q_e ($mg.g^{-1}$)	R^2	K_2 ($g.mg^{-1}.min^{-1}$	q_e ($mg.g^{-1}$)	R^2	
CAN-Chitosan	0,0323	31,6582	0,8929	0,0024	51,0204	0,9995	48,7598
CAN	0,0255	14,7833	0,7655	0,0039	51,8135	0,9993	50,5894

Table 4. Linear adsorption isotherm parameters of Cu^{2+} ions by CAN-Chitosan and CAN

Model	Parameter	Adsorbent	
		CAN-chitosan	CAN
Langmuir	K_L (L/mg)	0,1885	0,25
	q_{mL} (mg/g)	82,6446	78,125
	q_{mL} (mmol/g)	1,3006	1,2294
	R^2	0,9898	0,9816
Freundlich	K_f (L/g)	39,5367	42,4522
	n_f	7,0472	8,1633
	R^2	0,9948	0,8272
Sips	K_s (L/mg)	0,0000055	-
	n_s	0,1755	-
	q_{ms} (mg/g)	360,6529	-
	q_{ms} (mmol/g)	5,6759	-
	R^2	0,9911	-

Table 5. Non-linear adsorption isotherm parameters of Cu^{2+} ions by CAN-Chitosan

Model	Parameter	Metal
		Cu^{2+}
Langmuir	K_L (L/mg)	0.4073
	q_{mL} (mg/g)	75.8235
	q_{mL} (mmol/g)	1,1931
	SSR	782.5515
Freundlich	K_f (L/g)	38.6819
	n_f	6.7409
	SSR	22.4708
Sips	K_s (L/mg)	0,0000055
	n_s	0,1755
	q_{ms} (mg/g)	360,6529
	q_{ms} (mmol/g)	5,6759
	SSR	30.5811

Table 6. Comparison table of different adsorbents with the present study for Cu^{2+} removal

Adsorbent materials	Adsorption capacity (mg/g)	Reference
Zeolite NaP1	14.60	[74]
Zeolite NaP	42.90	[75]
Zeolite 4A	61.64	[53]
SCDO	24.32	[76]
Zeolite CAN	78,125	The present study
Composites CAN-Chitosan	82,6446	The present study